國立臺灣大學理學院大氣科學研究所

碩士論文

Department of Atmospheric Sciences
College of Science
National Taiwan University
Master's Thesis

海洋屏障層對颱風發展的影響之探討

Investigating the role of Ocean Barrier Layer on Tropical Cyclone Evolution

蕭柏智

Bo-Jhih Hsiao

指導教授：吳俊傑 博士

Advisor: Chun-Chieh Wu, Ph.D.

中華民國 114 年 7 月

July, 2025

doi:10.6342/NTU202502292

致謝

在高中時期，在老師的細心指導與悉心栽培下，我對地球科學這門學科逐漸產生了濃厚的興趣。其中，颱風作為一種極端天氣現象，尤其引起了我的熱情與關注。到了大學階段，我有幸加入吳俊傑教授領導的颱風動力研究室，展開了探索颱風動力學奧秘的學術旅程。在這個研究室中，我不僅享受到完善的研究環境與設備支援，得以進行深入的颱風相關研究，更結識了許多志同道合的學長姐，與他們一同交流心得、分享知識，並且能在平常的時候與他們聊颱風相關的趣事、哪一個颱風的眼牆比較大、颱風登陸台灣要不要去追風等等。

在研究方面，研究室的各位同仁為我的學術進程提供了無數寶貴的建議與幫助。我特別要感謝陶昱丞，他在實驗模擬等方面給予了我極大的支持與指導，若非他的協助，我的研究甚至可能無法順利啟動。我也感謝先嶸學長、明翰學長、俊愷學長及皓廷學長，在海洋模擬領域為我提供了多方面的靈感與思路，並對我的研究設計提出了具有深遠影響的見解與建議。此外，忠權學長、自雄學長、Peter 學長、宗勇學長以及里治學長，協助我處理研究室事務，使我能更加專心投入於研究工作，實在令人感動。同時，我想向 Benjamin 表達由衷的感謝，他不僅在研究方向上提供了重要支持，還在英文撰寫方面投入了大量心力，協助我提升摘要和論文的品質，使內容更加流暢和專業。此外，我也深深感謝金成學長、俊宇學長、宜萱學姊、逸鳴學弟、泓哲學弟以及子祐學弟，還有前述的學長姐們以及已離開研究室的學長姐們。他們在颱風動力研究室的 group meeting 中踴躍參與討論，尤其在我平時的報告和 pre-seminar 中提供了許多寶貴的建議和問題，幫助我不斷精進報告技巧，並在正式進行專題報告之前獲得更多準備的機會。最後，我要特別向吳俊傑教授表達誠摯的感謝。教授不僅為我的研究提供了明確的方向，也給予了大量的修改建議，並在論文撰寫的過程中提供了重要指導，使我的研究成果得以更加完善。

在這四年的大學生活與兩年的碩士旅程中，研究室的各位夥伴與教授為我的求學歷程增添了無數歡笑與溫暖。不論是在我的專題研究，還是平時的課程學習中，大家所分享的經驗與無私的付出讓我受益匪淺。在此，我再次感謝你們的陪伴與支持，若沒有你們，我或許無法取得如今的成就。此外，我要特別感謝一路以來始終支持我的家人。他們從小對我的細心栽培，對我的選擇的尊重與支持，讓我得以追尋自己熱愛的事物，並加入大氣系的學習之旅。因為有你們，我的成長與求學道路充滿了幸福與感激，謝謝。

doi:10.6342/NTU202502292

摘要

海洋結構的特性在颱風的演化中扮演了至關重要的角色。颱風施加的強風應力通過流切逸入和垂直混合作用將冷水從海洋下層拉出，進而降低海表面溫度，並減少颱風的最大潛力和當前強度，形成負反饋現象。垂直混合作用對颱風強度的影響越來越受到關注，尤其是颱風形成前的海洋剖面所扮演的角色。屏障層可以顯著增強海洋的穩定性，進而抑制海表面溫度的降溫效應，導致上層海洋熱含量的消耗。儘管一些研究已著重探討屏障層效應與颱風強度的關係，但深入探究屏障層與不同颱風強度的相關性仍然至關重要。因此本研究旨在進一步探索屏障層對颱風發展的影響。

本研究的目標是探討不同厚度的屏障層對颱風的影響，以及屏障層在不同颱風階段中對海洋結構和颱風強度的影響。我們使用耦合氣象研究與預報模型（WRF）和三維海洋模型 Price-Weller-Pinkel（3DPWP）進行理想化模擬，以簡化環境條件並聚焦於海氣交互作用和海洋變化。我們設置了具有四種不同屏障層厚度的初始海洋剖面，以分析這些模擬中颱風強度和海洋剖面變化的差異。

以上理想化模擬的結果顯示，屏障層對颱風的影響隨颱風強度而異。在環境條件良好且颱風已經較強的情況下，屏障層對颱風的發展影響較小。然而在不利條件下，如移動速度慢、輻射輸入減少以及中度或以上垂直風切的情況下，屏障層可能顯著影響颱風強度。未受擾動的屏障層因吸收短波輻射而顯示出變暖信號，且此效應隨屏障層厚度增加而增強。該過程強化了從海洋到颱風的表面熱通量傳遞，導致颱風增強。另一方面，對於弱颱風，混合層的降溫更加明顯且持久，削弱了颱風對於海表面熱通量的吸收作用，提供不利於颱風增強的條件。

關鍵字：熱帶氣旋的強度演變；SST 冷卻效應；混合層；屏障層；海洋鹽度分層；垂直混合作用；上層海洋熱含量；

doi:10.6342/NTU202502292

Abstract

The properties of ocean structure play a crucial role in the evolution of tropical cyclones (TCs). Strong wind stress exerted by TCs pulls cold water from the ocean underneath through entrainment and vertical mixing, cools down the SST and further decreases the maximum potential and current intensity of TCs, resulting in negative feedback. The impact of vertical mixing, which affects TC intensity, has gathered increasing attention, especially regarding the role of pre-TC ocean profile. Barrier layer (BL) can significantly enhance stability in the ocean column and ultimately suppress the SST-cooling effect, leading to the dissipation of upper ocean heat content. Although several studies have focused on the relationship between the BL effect and TC intensity, a comprehensive investigation into the correlation between the BL and varying TC intensities remains crucial. This study seeks to further explore the impact of BLs on the development of TCs.

The objectives of this study are to investigate the effect of BLs with different thicknesses on TCs and the influence of the BL on ocean structure and TC intensity during different TC phases. We use the Weather Research and Forecasting (WRF) model coupled with the 3D Price-Weller-Pinkel (3DPWP) ocean model to conduct idealized simulations to simplify environmental conditions and to focus on the examination of the air-sea interaction and ocean variation. Different initial ocean profiles with four BL thicknesses are set to investigate the differences in TC intensity and changes in ocean profiles among these simulations.

Results from the above idealized simulations indicate that the influence of BLs on TCs varies with TC intensity. BLs have a minimal impact on TC development when environmental conditions are favorable and TCs are already strong. However, under unfavorable conditions—such as slow movement, reduced radiation input, and moderate or strong vertical wind shear—BLs can significantly influence the TC intensity. An unperturbed BL shows a warming signal due to the absorption of shortwave radiation, with this effect intensifying as BL thickness increases. This process enhances surface heat flux transfer from the ocean to the TCs, leading to accelerated

doi:10.6342/NTU202502292

intensification. On the other hand, for weak TCs, the cooling in the mixed layer becomes more pronounced and prolonged, reducing surface heat flux uptake and resulting in more unfavorable conditions for intensification.

Key words: Tropical cyclone intensity evolution; SST cooling effect; Mixed layer; Barrier layer; Ocean salinity stratification; Vertical mixing; Upper ocean heat content

doi:10.6342/NTU202502292

Table of contents

doi:10.6342/NTU202502292

doi:10.6342/NTU202502292

List of Tables

doi:10.6342/NTU202502292

List of Figures

doi:10.6342/NTU202502292

doi:10.6342/NTU202502292

doi:10.6342/NTU202502292

doi:10.6342/NTU202502292

doi:10.6342/NTU202502292

doi:10.6342/NTU202502292

doi:10.6342/NTU202502292

Chapter 1

Introduction

1.1 The factors associated with tropical cyclone intensification

Tropical cyclone (TC) intensification is governed by a constellation of interconnected atmospheric and oceanic factors. On the atmospheric side, a key element is weak vertical wind shear (VWS), which helps maintain the storm's structural integrity. Many studies have done thorough investigation in the relationship between various VWS and different phases of the TCs. For example, mechanisms such as vortex tilt reduction and the establishment of precipitation symmetry counteract disruptive shear effects, allowing TCs to preserve their core even under moderate shear conditions (Rios-Berrios et al. (2024)). Equally important is the presence of a moist mid-troposphere. A humid mid-level environment diminishes the risk of dry air intrusion and sustains vigorous diabatic heating through enhanced latent heat release. Meanwhile, upper-level divergence facilitates the evacuation of air from the core of the TCs, promoting the inflow of warm, moist air at lower levels and further stabilizing the cyclone's development (Leroux et al., 2013). In addition to the environmental conditions, the internal dynamics of TCs, such as convective bursts and eyewall replacement cycles, also play a critical role in the storm's intensification. These processes, which reflect the evolving symmetry and energy distribution within the cyclone, have been shown to correlate strongly with rapid intensification phases, underscoring that the internal structure can adapt in response to environmental forcing (Tao & Zhang, 2019). In essence, the interplay between external environmental conditions and these adaptive internal processes creates a feedback loop

doi:10.6342/NTU202502292

that often accelerates intensification, making the study of these interactions central to understanding the behavior of TCs.

In addition to atmospheric influences, the ocean's pre-storm state is equally critical for the formation and intensification of TCs. Observational studies show that when sea surface temperatures exceed roughly 26–26.5 °C, they sustain the heat and moisture fluxes that drive storm development (Emanuel 1986). Therefore, elevated surface sea temperatures (SSTs) have been linked to sustained intensification rates where the regions with higher SST can continually support greater intensification rate for developing TCs. According to the historic records, Hurricane Katrina (2005) underwent explosive strengthening over Gulf of Mexico waters warmer than 30 °C, rapidly reaching Category 5 status (McTaggart-Cowan et al. 2007). In the tropical Atlantic basin, Hurricane Harvey (2017) underwent a pronounced phase of rapid intensification as it moved over anomalously warm Gulf of Mexico waters, where SSTs approached 30 °C, providing the enthalpy flux necessary for its escalation to a major hurricane. Likewise, in the western North Pacific, Super Typhoon Haiyan (2013) traversed a region with surface temperatures exceeding 29 °C, a thermally supportive environment that underpinned its record-breaking intensification into one of the strongest TCs on record (Wang et al. 2018). In support of these findings, Yablonsky and Ginis (2013) highlighted the role of warm-core eddy providing substantial heat to the upper ocean, further reducing SST cooling and enhancing the storm's energy supply. Together, these insights not only show the importance of the ocean thermal structure on TC development, but also underscore the critical importance of integrating both atmospheric and oceanic perspectives in understanding TCs dynamics and improving forecasting accuracy.

1.2 SST-cooling effect

doi:10.6342/NTU202502292

The air-sea interaction between the ocean and TCs plays a crucial role in storm intensification by governing ocean heat uptake. A comprehensive understanding of this interaction is essential for improving the accuracy and reliability of TC forecasting. Previous research has demonstrated that cyclonic surface wind stress generated by TCs can induce the mixing of cooler water from deeper ocean layers into the upper ocean via entrainment and vertical mixing processes. This mechanism results in a reduction of sea surface temperature (SST), commonly referred to as the SST-cooling effect (Price 1981, 1994; Emanuel 1986; Shay et al. 1989; Lin et al. 2003b, 2013; Wu et al. 2007, 2016; Chang et al. 2023).

This cooling is primarily driven by the enhanced interaction between wind stress and ocean currents. For instance, Wu et al. (2016) showed that Typhoon Megi's passage in the South China Sea led to significant SST cooling, which in turn was directly linked to a reduction in storm intensity. Factors such as storm translation speed, surface wind stress, and the upper-ocean thermal structure all play crucial roles. The ocean's response can be understood in terms of Ekman dynamics and quantified using bulk formulas (Garratt 1977). In this framework, the strong wind stress imposed by a TC creates an Ekman pumping effect that varies with depth, as captured by Equation (1-1):

$$\vec{\tau} = \rho_a C_D \left|\vec{U}\right| \vec{U} \quad (1\text{-}1)$$

where τ is the surface wind stress, ρ_a is the air density, C_D is the neutral drag coefficient which is related to the logarithmic wind profile in the surface layer, and U is the wind speed measured at a reference height (typically 10 m). Price et al. (1994) further suggested that the maximum depth reached by the TC-induced mixing is controlled by the wind stress magnitude, as represented by Equation (1-2):

$$W_{-h_{MLD}} = \frac{1}{\rho f}(\nabla \times \vec{\tau}) \quad (1\text{-}2)$$

doi:10.6342/NTU202502292

where the left side of the equation stands for the vertical velocity at the base of the ML, ρ is the density of seawater and the f is the Coriolis parameter. This equation suggests that the TC induced vertical mixing is dependent with TC intensity, impling that that stronger wind stress produces deeper mixing, effectively setting a limit on the ML depth through turbulent entrainment. Therefore, the strong wind stress generated by the TC exerts a force on the ocean surface, transferring momentum into the water. This wind-induced momentum initiates motion not only in the direction of the wind but also leads to a spiral structure of currents with depth, known as the Ekman spiral.

The strong wind stress generated by TCs drives an upper-ocean current response that is systematically deflected relative to the storm's track. In the Northern Hemisphere, this response is shifted to the right of the cyclone's path (and to the left in the Southern Hemisphere), as demonstrated by Price et al. (1994). Their study of TC Gloria (1985) revealed an asymmetric SST cooling pattern, with cooling exceeding 2°C on the right side of the track compared to roughly 1°C on the left. This asymmetry arises because the Coriolis force acts perpendicular to the motion of moving water, leading to a net Ekman transport that is deflected 90° to the right in the Northern Hemisphere. Consequently, as the storm progresses, the region immediately to the right receives a greater momentum influx, enhancing vertical mixing and resulting in more pronounced SST cooling. This differential cooling, in turn, influences the efficiency of heat exchange between the ocean and the atmosphere, producing an observable cold wake centered along the cyclone's track—with particularly strong cooling on the right side.

In addition to lateral differences, the strength of SST cooling near the TC center is also modulated by the storm's translation speed. Under slow translation (around 2–3 $m\ s^{-1}$), the prolonged residence time allows wind stress to act more effectively on entraining deeper, colder water through Ekman pumping. Wu et al. (2007, 2016)

doi:10.6342/NTU202502292

demonstrated that this sustained interaction deepens the ML, which promotes direct mixing with cold thermocline water and reinforces the SST-cooling effect. Correspondingly, Wei et al. (2018) found that variations in surface heat flux (SHF) significantly contribute to SST cooling using in situ observations and reanalysis data. As the SST falls, the resulting decrease in SHF diminishes the ocean's capacity to supply heat, thereby imposing negative feedback on TC intensification (Emanuel 1986; Shay et al. 1989).

This integrated view links wind-induced mixing, Ekman dynamics, SST cooling, and SHF variations, demonstrating the critical importance of accurately representing ocean coupling in both observational studies and numerical simulations of TCs.

1.3 Upper Ocean heat content (UOHC)

Since vertical mixing induced by TCs can entrain cold water from the deeper layer, it is essential to consider not only SST but also the integrated heat content of the upper ocean, commonly referred to as upper ocean heat content (UOHC), when evaluating the energy available for TC intensification. UOHC serves as a measure of the thermal energy stored within the ocean's mixed layer (ML) and sub-surface, which directly influences the fluxes of heat and moisture into the atmosphere that drive cyclone intensification.

Lin et al. (2013) demonstrated that the impact of the SST-cooling effect diminishes with higher initial UOHC, showing that the deep reservoir of warm water can counteract the cooling resulting from storm-induced mixing, thereby sustaining the air–sea energy exchange necessary for further intensification. When high UOHC is present, TCs passing through these regions are more likely to encounter a continuous supply of high-energy water, reducing the negative feedback from SST cooling effect. This suggests that regions

doi:10.6342/NTU202502292

with a deep, warm ocean water column have the ability to sustain the energy supply for the TCs. Therefore, it underscores that the depth and thermal characteristics of the ML are critical determinants of whether a TC can undergo prolonged strengthening or even explosive intensification.

Furthermore, a high UOHC not only provides the heat necessary for cyclone development but also enhances the resilience of the ocean to SST-cooling. In other words, the thermal characteristics and the thickness of the ML are key deciding factors restricting the magnitude of cooling in whether a TC undergoes prolonged strengthening or explosive intensification, effectively limiting the cyclone's self-induced negative feedback, indicating that the enhanced UOHC supports the air-sea heat exchange which is necessary for TC intensification. This concept is supported by studies such as Shay et al. (2010), Lin et al. (2013), and Chandra and Kumar (2021), which collectively suggest that enhanced UOHC reinforces the air-sea interaction to supply sufficient heat to the overlying cyclones, thereby maintaining or even accelerating its intensification.

Overall, these findings highlight the importance of thoroughly understanding not only the temperature change of the SST but also the initial vertical ocean thermal structure prior to the arrival of a TC. Thus, a comprehensive assessment of the ocean column's condition before the arrival of the TCs is critical for improving forecasting of both cyclone intensity and storm surge impacts.

1.4 Ocean properties

The stability of the ocean profile plays a critical role in influencing the extent of TC-induced vertical mixing. Understanding the temperature and salinity profiles at each layer, both horizontally and vertically, is crucial for ocean model simulations and for

doi:10.6342/NTU202502292

understanding TC-induced air-sea interaction in this study. The classical theory or simulations focusing on TC intensification often treat the upper ocean as a two-layer system. In this framework, above the depth of the ML is assumed to be well mixed in both temperature and salinity, while the underlying thermocline is characterized solely by thermal stratification. Due to a nearly constant density within the ML, TCs can rapidly entrain cold water from the thermocline into the well-mixed upper layer, thereby inducing an immediate SST cooling effect. Moreover, reviews and modeling studies have adopted this simplified upper-ocean structure to investigate TC intensification mechanisms (e.g., Stewart, 2004) and feedback from ocean (e.g., Price 1981).

Several studies have identified regions in the global ocean where notable discrepancies between thermocline and pycnocline depths are observed (e.g., Lukas and Lindstrom, 1991; Sprintall and Tomczak, 1992). The overlying layer, termed the barrier layer (BL), develops in areas with pronounced salinity gradients within specific upper ocean layers and was initially discovered in the western equatorial Pacific. The formation of the pronounced salinity gradient is mainly attributed to the freshwater inputs such as evaporation/precipitation imbalance and discharge from the river plume. George et al. (2019) highlights that heavy rainfall and river runoff produce a fresh, low-salinity surface ML through in situ microstructure measurements, showing that the surplus freshwater input intensifies the salinity gradient between the surface and deeper layers, promoting a more robust and persistent BL. The former often occurs in the tropical regions where consistently heavy rainfall such as in the equatorial Pacific can lead to the formation of a BL by diluting the surface salinity and restricting vertical mixing (You, 1998). The presence of a low-salinity surface layer causes the depth of the uniform-density ML to be shallower than the isothermal layer (IL). Sprintall and Tomczak (1992) and Kara et al. (2000) demonstrated that the formation of the BL extending across the Northwest Pacific

doi:10.6342/NTU202502292

is primarily driven by thermocline deepening due to local freshwater fluxes combined with an increased imbalance between precipitation and evaporation during winter at the surface. De Boyer Montégut et al. (2004) analyzed extensive temperature and salinity profiles from 1941 to 2002 and pointed out a pronounced BL thickness in the Amazon-Orinoco region, largely influenced by freshwater inputs from the Amazon and Orinoco Rivers into the Caribbean.

The presence of the BL enhances upper ocean stability with density gradients arising from temperature and salinity differences contributing to stratification, thereby modulating the extent of TC-induced vertical mixing and influencing air-sea interactions. Numerous studies have suggested that variations in SHF can contribute to TC intensification under specific conditions. (Balaguru et al. 2012; Reul et al. 2014a; Yan et al. 2017; Hlywiak and Nolan 2019). Balaguru et al. (2012) demonstrated that TC Omar (2008) in the Caribbean Sea underwent intensification due to the presence of the BL, suggesting that the diminished effectiveness of vertical mixing leads to a reduced SST-cooling effect, which subsequently influences TC evolution by altering air–sea interaction. Furthermore, the characteristics of the pre-TC ocean profile and the properties of the TC, including intensity, size and transition speed, are important factors for the BL's influence on TC intensity. Stronger TC intensity and extended residence time promote more pronounced vertical mixing within the upper ocean. Hlywiak and Nolan (2019) examines various BL thicknesses and environmental factors through idealized ensemble simulation, concluding that increased BL thickness enhances ocean stability, supports higher SHF, and results in greater TC intensity.

doi:10.6342/NTU202502292

1.5 Motivations and the scientific objectives

Yan et al. (2017) investigated the influence of BLs on the upper-ocean structural response, specifically SST cooling and ML deepening, during TC passage. However, their study conducted a one-way forced framework, prescribing an idealized cyclone wind field and employing a one-dimensional Price–Weller–Pinkel (1DPWP) ocean model. Although this configuration enables examination of ML thermodynamics, it cannot assess how BLs modulate cyclone intensity evolution under varying environmental conditions. Furthermore, several studies (e.g., Balaguru et al. 2012; Hlywiak and Nolan 2019) have demonstrated that the presence of a BL in air–sea interactions enhance oceanic stability and thereby attenuates the SST-cooling effect. Nevertheless, it remains unclear whether BLs invariably provide positive feedback on TC intensity throughout the distinct phases of storm evolution under different environmental conditions. To address these gaps, we explore the phase-dependent impacts of BLs by investigating how varying BL thicknesses affect cyclone intensification in this study. Specifically, our objectives are twofold: (1) to examine the effects of BLs with varying thicknesses on TC intensity and (2) to analyze the impact of BLs on TCs at various stages of development, including the underlying physical processes that govern these interactions.

To address these objectives, we employ a fully two-way ocean-coupled, idealized simulation framework designed to assess the evolution of the upper ocean structure in response to TC passage under varying initial BL conditions. Detailed descriptions of the model configuration and methodology are provided in the next section. Section 3 discusses the results pertaining to TC evolution and the corresponding SST variations across different BL thickness scenarios. In Section 4, we present comparative analyses and quantify changes in ocean properties and UOHC. In-depth discussions, conclusions, and directions for future work are outlined in Section 5 in order.

doi:10.6342/NTU202502292

Chapter 2

Data and Methodology

2.1 Model description

The numerical simulations conducted in this study are conducted using the Weather Research and Forecasting (WRF) Model version 4.3.3. The WRF model is coupled with the three-dimensional, time-dependent Price-Weller-Pinkel (3DPWP) ocean model (Price 1994). The 3DPWP ocean model robustly simulates horizontal and vertical ocean currents, temperature profiles, and various other oceanic properties at high temporal resolution. By employing this coupled framework, we can systematically investigate the response of ocean temperature and salinity profiles, as well as the evolution of the ML with different BL thickness scenarios during TC passage. This approach provides a comprehensive platform for analyzing the impact of BL characteristics on TC intensity trends in idealized simulations across diverse oceanic conditions. Wu et al. (2007, 2016) highlight the critical role of ocean coupling in WRF simulations, as TCs in these simulations tend to intensify excessively under conditions of constant high SST. By incorporating modifications to the ocean model, the negative feedback from SST cooling effectively regulates the heat flux between the ocean and the atmosphere, yielding results that align more closely with observations. Further details on the model are available in Price et al. (1994).

2.2 WRF model initial configurations

To examine the influence of BLs on TC intensity, we perform a series of idealized numerical experiments. Each simulation is initialized with a low-level atmospheric vortex

doi:10.6342/NTU202502292

characterized by a maximum wind speed (V_{max}) of 20 m s^{-1} and a radius of maximum wind (RMW) of 90 km, centered at 20˚N. The simulations employ a two-domain configuration on a beta plane: a fixed outer domain (d01) with a horizontal resolution of 10 km and an inner, nested moving domain (d02) with a resolution of 3.3 km.

To accommodate the 3DPWP ocean model's minimum resolution requirement of 3 km, the resolution for the inner, d02 is set slightly above this threshold. D01 comprises 889 × 556 grid points with periodic boundary conditions, while the d02 consists of 400 × 400 grid points and is configured to continuously track the vortex center at the 700-hPa level. The atmospheric vertical structure consists of 30 levels in pressure coordinates, extending upward to a height of 22.5 km. Each simulation runs for a 6-day period with a 45-second time step for both domains, and output is generated on an hourly basis. The microphysics scheme is configured using WDM6. Shortwave and longwave radiation schemes are implemented with the RRTM scheme and Dudhia scheme, respectively, to effectively capture the diurnal cycle's influence on surface ocean heat uptake. Additionally, the boundary layer is parameterized using the YSU scheme, and cumulus convection is represented by the Kain-Fritsch scheme. These configurations serve to minimize extraneous variables that could otherwise affect air–sea interactions and the overall oceanic response.

Several studies and observations indicate that the magnitude of the negative feedback ocean response induced by a passing TC depends on various factors, including the initial profile of the ocean column, as well as the size, intensity, and translation speed of the TC. These factors determine the duration and impact of wind stress on the ocean (Shay et al. 1989). According to Feng (2024), the observed climatological translation speed of TCs is approximately 5 m s^{-1} within the latitudinal range of 10˚N to 30˚N. Therefore, to assess sensitivity of translation speed to TC intensity, we design the experiment with a uniform

doi:10.6342/NTU202502292

eastward steering flow (SF) of 2 m s^{-1} and 5 m s^{-1}, which are denoted with "SF02" and "SF05" at the front of the experiments' names, respectively. This setup, achieved by implementing time-varying point downscaling (TVPDS), effectively represents both slow and moderate TC translation speeds (Fig. 2.1), thereby enabling us to assess the impact of translation speed variations on TC intensity.

In addition to the characteristics of the TC, environmental factors, such as net shortwave radiation and wind shear, are critical to TC development. To assess the sensitivity of TC evolution to these variables, we repeat simulations with uniform SFs while systematically varying shortwave radiation and environmental wind shear. It is important to note that, due to the periodic boundary condition and the absence of the ocean currents in these ideal simulations, the ocean continually absorbs incoming shortwave radiation, causing the near-surface temperature to progressively increase over the simulation period. To mitigate the impact of shortwave radiation on ocean temperature, repeated simulations are adjusted by altering the simulation period from September to October and shifting the initial TC center northward to 25˚N. Simulations modified to reduce shortwave radiation are designated with the suffix "-LSW" in the experiment names.

Vertical wind shear (VWS) is another critical factor in impacting TC intensity because it disrupts a storm's symmetric structure and reduces its intensification potential. In their climatological analysis, Rios-Berrios and Torn (2017) emphasized the importance of storm-relative and environmental characteristics in understanding intensity changes under moderate VWS conditions. Their study indicates that, during TC seasons in the WNP, the typical eastward wind shear is approximately 7 m s^{-1}. This moderate shear influences TC evolution by affecting the tilt and organization of the storm's core, thereby modulating its intensification potential. To assess the sensitivity to TC development, uniform wind

doi:10.6342/NTU202502292

shear is introduced in repeated simulations alongside adjustments to shortwave radiation. Simulations modified with moderate VWS are denoted with the suffix "-VWS" appended to the original experiment name. (See Table 2.1).

2.3 Ocean structure initial settings

The three-dimensional Price-Weller-Pinkel (3DPWP) model is employed within the WRF framework to simulate air-sea interactions and construct the initial temperature and salinity profiles. Figure 2.2 illustrates the variables associated with the initial ocean structures. The design of the initial ocean settings is inspired by the work of Hlywiak and Nolan (2019). In all simulations, the ocean model spans from a depth of 2 m to 296 m, discretized into 30 vertical levels. To accurately resolve the dynamics of the near-surface layer, a finer vertical resolution of 6 m is used from the surface down to 104 m. For the deeper layers, where high resolution is less critical, a coarser vertical interval of 16 m is employed.

Figure 2.2a illustrates the initial temperature profile as a function of depth. The temperature remains constant from the surface down to 46.4 m, defining the extent of the IL, as indicated by the dashed line. Below 46.4 m, a lapse rate of 0.1 °C m^{-1} is applied until the temperature reaches 4 °C. The settings of the ocean temperature in each experiment can be categorized as T27, T28, and T29, respectively, regarding to the temperature within IL. As shown in Fig. 2.2b, the salinity structure is modeled using a hyperbolic tangent function to ensure continuity and reaches a constant value of 35 psu in the deeper layers. According to Li et al. (2019), the surface salinity of the Pacific Ocean typically ranges between 34 and 35 psu. However, near coastal regions, surface salinity decreases when influenced by freshwater deposition. Therefore, the initial surface salinity

doi:10.6342/NTU202502292

values are set to 31, 32, 34, and 35 psu. Figure 2.2c presents the corresponding potential density, which increases with depth as a function of temperature, salinity, and pressure, in ocean structure, representing with the configuration from group T28. It shows that under constant temperature, lower salinity leads to a lower potential density. Finally, Figure 2.2d presents the corresponding Brunt-Väisälä frequency with respect to depth, which represents with the configuration from group T28, demonstrating that ocean stability is primarily enhanced by salinity gradients that form the BLs. The definition of Brunt-Väisälä frequency in the ocean is computed in Gibbs SeaWater Oceanographic Toolbox (GSW) via the 75-term polynomial for specific volume, which is outlined in equation (2-1). At pressure mid-points, it is given by:

$$N^2 = \frac{g}{specvol_{mid}\Delta P_{Pa}}(\alpha_{mid}\Delta CT - \beta_{mid}\Delta SA) \quad (2\text{-}1)$$

, where ΔP_{pa} is the pressure difference between each layer, $specvol_{mid}$, α_{mid}, β_{mid} are specific volume, thermal expansion and saline contraction coefficients at the mid-level of each layer, CT is conservative temperature, and SA is absolute salinity. Conservative temperature is a variable that corrects for non-conservative behavior of in situ or potential temperature, ensuring a physically consistent heat content metric when comparing profiles at different salinity and pressure. A pronounced salinity gradient occurs between 14 and 38 m, resulting in a maximum Brunt-Väisälä frequency of 25 cycles per hour (cph) for a BL thickness of 30 m. Below the depth of the IL, since the temperature decreases at a constant lapse rate of 0.1 °C m^{-1} (until reaching 4 °C) and salinity remains fixed at 35 psu; as a result, the corresponding vertical profiles of potential density and Brunt–Väisälä frequency coincide. Therefore, Figure 2.2 concentrates on the upper ocean structure, highlighting the pronounced salinity gradient and the associated stability enhancement. The spatial resolution is set identical to that of the WRF model,

doi:10.6342/NTU202502292

with time steps provided at a 1-minute time resolution. The initial ocean is set to be quiescent, meaning there are no pre-existing currents or sea surface height anomalies. As a result, any currents that develop during the simulations can be attributed exclusively to the wind stress generated by the TCs.

2.4 Definition of the ocean layers

The thickness of the BL is defined as the difference in depth between the IL and the ML (Balaguru et al, 2012; Chu and Fan, 2023). Several studies have proposed different criteria to the definitions of both IL and ML employing either temperature-based or density-based approaches (Lukas and Lindstrom, 1991; Sprintall and Tomczak, 1992; Vialard and Delecluse, 1998a; Hlywiak and Nolan, 2019). Since our simulation primarily focuses on the effect of the BL form by the salinity stratification in the ocean, therefore, we adopt the density-based criteria described by De Boyer Montégut et al. (2004) and Hlywiak and Nolan (2019)**.** Specifically, the depth of the IL is defined as the depth at which the temperature differs from a near-surface reference value at 10 m by a specified amount, as outlined in Eq. (2-2). Similarly, the depth of the ML is determined based on a density criterion, where the ocean's potential density increases by a defined amount relative to the near-surface reference value, as detailed in (see Eq. (2-3)). This increment corresponds to the density change resulting from a temperature drop of 0.2°C in seawater with constant salinity conditions. The ocean structure which includes the BL can be illustrated as Fig. 2.3.

$$\delta T = T_{z\,=\,Depth\ of\ the\ IL} - T_{10m} < -0.2℃ \quad (2\text{-}2)$$

$$\delta\sigma_t = \sigma_t(T + \delta T, S, P) - \sigma_t(T, S, P) \quad (2\text{-}3)$$

doi:10.6342/NTU202502292

According to Table 2.1, a total of 72 simulations are conducted, with each experiment initiated using an identical vortex. These simulations are generated by the combinations of 6 environmental factors, which is achieved by controlling SF, shortwave radiation, and VWS in WRF, with 4 different BL thickness options and 3 unique initial temperature profiles in 3DPWP.

doi:10.6342/NTU202502292

Chapter 3

Results --- TCs evolution and corresponding SST variation

3.1 Evolution of TC intensity

The evolution of TCs intensity across experiments, as illustrated in Fig. 3.1, reveals substantial variability driven by environmental factors. Favorable environmental conditions, such as low VWS and high SST, promote a faster intensification rate of the TCs (Guo et al. 2024). Figure 3.1 demonstrates that TCs intensify from a maximum velocity of 20 m s^{-1} to a range of 40–60 m s^{-1} or higher, depending on SST. Notably, experiments in group T29 show that elevated SSTs yield not only higher peak intensities but also more rapid intensification, emphasizing the critical role of thermal energy in cyclone development. Conversely, group T27 exhibits delayed intensification and reduced maximum intensities under less favorable conditions. The results establish that high SSTs not only provide the essential energy for cyclone development but also modulate the rapid intensification process and thereby encouarge stronger storms with larger maximum potential intensity corresponding with several studies (Bhatia et al. 2018, Xu and Wang 2018). Furthermore, faster translation speeds enhance TC intensification by mitigating the SST cooling effect, while slower speeds exacerbate cooling due to longer residence times over a given ocean region (Wu et al. 2007, 2016). When comparing TCs under identical environmental conditions, such as in SF02-LSW (Fig. 3.1b) and SF05-LSW (Fig. 3.1e), comparisons between slow and moderate translation speeds reveal that TCs with a faster (moderate) translation speed exhibit a stronger intensity than those with a slower translation speed, revealing that faster-moving TCs intensify more rapidly,

doi:10.6342/NTU202502292

in agreement with earlier findings. Findings above can also be seen in comparison between other experiments. Several studies have shown that translation speeds below approximately 4–5 m s^{-1} induce more pronounced SST cooling. In other words, a shorter residence time over the cold wake region enables TCs to move away before the cooling effect fully develops, thereby reducing its impact on air–sea heat exchange. In the SF05-LSW-VWS simulation (Fig. 3.1f), which incorporates an additional VWS parameter, the results underscore its critical role in modulating ocean temperature. However, unfavorable environmental conditions result in a significantly lower TC intensity compared to the SF05-LSW simulation, where VWS is the sole variable. Moreover, a direct comparison between the SF05 and SF05-LSW simulations demonstrates that diminished shortwave radiation input further contributes to a decrease in TC intensity (Figs. 3.1d and e). These observations collectively suggest that both alterations in shortwave radiation and the incorporation of VWS critically shape the evolution of TCs, with the supplementary VWS parameter exerting a more pronounced impact. Furthermore, when comparing SF02-LSW and SF05-LSW-VWS, although the slower translation speed in SF02-LSW yields a larger ocean response, the influence of VWS on TC intensity is more pronounced that will influence the air-sea interaction and the ocean response.

Among all simulations, those conducted under favorable environmental conditions (SF02, SF05, and SF05-LSW) exhibit rapid intensification, particularly within the high-SST group (T29), and quickly attain equilibrium state (Figs. 3.1a, d, and e). The rate of intensification is sufficiently high that BLs become relatively ineffective to strong vertical mixing, such that their impact on TC intensity is minor compared to that of favorable environmental conditions. Consequently, the effect of BLs during the weaker stages of cyclone development is difficult to isolate and examine in these experiments. By contrast,

doi:10.6342/NTU202502292

the SF02-LSW-VWS experiment, which features pronounced vertical wind shear and reduced shortwave forcing, fails to generate a TC from the initial vortex excepted for T29 group. In addition, its slow translation speed further amplifies SST cooling and deprives the system of oceanic heat supply, ultimately leading to storm dissipation (Fig. 3.1c). Consequently, to thoroughly investigate the impact of the BLs on evolution of the TCs, the following discussion will mainly focus on a detailed comparison between the SF02-LSW and SF05-LSW-VWS experiments and the mechanisms driving their divergent outcomes.

Higher SST along the trajectory of TCs substantially enhances both their intensification rate and maximum intensity, suggesting that both energy availability and TC motion are crucial in determining the maximum intensity of TCs. In terms of salinity's influence, a thicker BL, which is typically associated with denser salinity stratification, reinforces ocean stability, leading to the regulation of air–sea interactions and adjustment in heat fluxes. Unlike parameters that directly affect TC structure or heat exchange, BL thickness primarily alters the rate of vertical mixing and the corresponding temperature variability.

As shown in our simulations, under favorable environmental conditions (e.g., SF05-LSW in Fig. 3.1e), the findings show that the TCs intensify rapidly such that the stabilizing effect of a thicker BL exerts only a minimal impact. Conversely, under unfavorable conditions (as illustrated in Figs. 3.1b and 3.1f), the thickness of the BL emerges as a crucial factor in determining TCs intensification. Simulations SF02-LSW and SF05-LSW-VWS reveal that thicker BLs have markedly influence on the TC intensification. In the SF02-LSW simulation, the experiment featuring a thicker BL (BLT30) shows markedly stronger intensification within group T29 compared to other configurations, whereas within group T27, a thicker BL corresponds with lowering

doi:10.6342/NTU202502292

maximum intensities. Similarly, in the SF05-LSW-VWS simulation, both groups T28 and T29 consistently exhibit reduced and postponed TC intensification as the BL becomes thicker. Specifically, during the simulation period from 72 to 144 hours, these results indicate that thicker BLs enhance the intensification rate for systems already achieving high TC intensity, yet dampen the rate for weaker systems, with 40 m s^{-1} being the delineating threshold. These contrasting outcomes suggest that the influence of BL thickness on TC intensification is highly dependent on the existing environmental context and inherent storm strength. Therefore, to further examine how BL thickness affects TC intensity in the ocean response, our upcoming parts will primarily focus on simulations conducted under unfavorable conditions.

3.2 The variation of SST and SHF

While slower translation speeds tend to amplify the SST cooling effect, our results indicate that during the period of increasing intensity, the presence of a thicker BL mitigates SST cooling by suppressing vertical mixing depth (Fig. 3.2). Specifically, as illustrated in Fig. 3.2a, the presence of the BL reduces the overall SST cooling, resulting in higher SST values compared to the BLT00 case. In the absence of a BL, SST cooling can exceed 2˚C, as demonstrated in scenario T29. Conversely, when thicker BLs are present, pronounced suppression of SST cooling occurs across all scenarios over time. Additionally, the difference in SST increases, with the cooling suppression reaching up to 1.5˚C in the SF02-LSW case. Correspondingly, the suppression of the SST cooling is coupled with an increased SHF uptake, ranging from 200 to 400 W m^{-2} compared to conditions without a BL. Given the positive correlation between SHF, SST, and TC

doi:10.6342/NTU202502292

intensity, the presence of thicker BLs results in higher SHF, thereby creating a more favorable environment for enhanced TC intensification (Fig. 3.3a).

On the contrary, in experiments SF05-LSW-VWS (excluding group T27) and group T27 of SF02-LSW, the presence of the BL under weak TC intensity results in a different response compared to SF02-LSW, manifesting as a decreased or delayed intensification. Here, due to the moderate translation speeds in SF05-LSW-VWS, the SST cooling effect is less pronounced than in SF02-LSW. In the absence of a BL, SST cooling can only reach approximately 0.7˚C, as demonstrated in scenario T29. When thicker BLs are present, the results also show pronounced suppression of SST cooling effect across all scenarios, with BLT30 exhibiting only minimal SST changes. Therefore, the presence of a BL in this experiment also notes the further mitigation of the SST cooling effect by inhibiting vertical mixing (Fig. 3.2b). However, the pattern in SHF differs markedly from that observed in SF02-LSW. Although cases with the presence of the BL exhibit a suppression in the SST cooling effect and maintain relatively high value, the corresponding SHF uptake shows an opposite trend. With a thicker BL, the SHF is lower compared to BLT00, with a maximum difference ranging from 200 to 400 W m^{-2}. The counterintuitive outcome is attributed to reduced latent heat flux due to the weaker TC intensity, ultimately providing unfavorable conditions for intensification (Fig. 3.3b). These different outcomes from SF02-LSW and SF05-LSW-VWS under the presence of the BL will be discussed in the following sections. Together, these simulations demonstrate that while BLs consistently suppress vertical mixing, their overall effect on TC intensification depends critically on the translation speed and the prevailing storm intensity.

doi:10.6342/NTU202502292

Chapter 4

Results --- Comparative analysis in ocean properties

4.1 Temperature change in the ocean column following TC center

Lin et al. (2003) emphasizes that the upper ocean heat content (UOHC) represents an important factor for the further intensification of TCs. To understand the significant differences in the influence of BLs between experiments SF02-LSW and SF05-LSW-VWS, it is necessary to analyze not only the near-surface conditions but also the temperature changes throughout the entire ocean column. The timing and magnitude of SST cooling are strongly dependent on the maximum mixing depth induced by TCs and the temperature profile preceding their arrival. Given that the influences of BLT12 and BLT24 fall between those of BLT30 and the absence of BL, our discussion of ocean temperature changes is confined to the BLT30 and BLT00 experiments. Figures 4.1a, b illustrates the changes in ocean temperature throughout the entire column, tracking the center of TCs in experiment SF02-LSW. Since the results from group T28 lie between those from groups T27 and T29, only the data from group T28 are used to represent the temperature changes.

During the initial 72-hour simulation period, the cooling pattern in the BLT30 experiment indicates that the vertical mixing induced by a weak TC is not strong enough to penetrate the BL (Fig. 4.1b). Consequently, vertical mixing has been inhibited within the ML, resulting in an increasing warming trend over time at depths between 20 and 50 meters, which corresponds to the location of the BL, while a cooling trend prevails in the remainder of the ML. In this scenario, the cooling within the ML reflects the signal of the diurnal cycle and becomes more pronounced as the BL thickness increases, compared to

doi:10.6342/NTU202502292

cases where the BL is absent. Because vertical mixing is insufficient to entrain cold water below the IL during this simulation period, ML cooling can be attributed primarily to air-sea heat loss, which transfers thermal energy from the upper ocean to the atmosphere (Price 1981, Vincent et al. 2012, Yan et al. 2017). Moreover, as the IL deepens, the warming below the IL intensifies with the strengthening of the TC. In the absence of entrainment below the base of the ML due to the weak induced vertical mixing, the IL base which defined as the depth where temperature first falls below the reference level within the ML by a certain value (see Eq. 2-2), would ordinarily remain fixed. However, since the IL isotherm is tied to the ML temperature, any cooling of the ML lowers the corresponding isotherm, causing the IL base to descend. During the first 72 hours of TC intensification, gradually enhancing vertical mixing drives significant ML expansion, yet the decrease in ML temperature remains relatively small. Consequently, the IL deepens alongside the ML but at a slower rate, reflecting the balance between isotherm adjustment and turbulent mixing. By contrast, in the same depth range, the BLT00 configuration exhibits the typical cooling pattern observed within the ML and warming below the IL, without any warming signal in the 20-to-50-meter depth range (See Fig. 4.1a). Without the high stability within the BL, the ML and IL become deepen at the same rate.

Under the BLT30 configuration, during the range of 72-96 hours, as the TC intensifies to roughly 35-40 m s^{-1}, the simulation results reveal a notable suppression of the warming signal within the BL (Fig. 4.1b). This occurs because the ML deepens more rapidly than the IL, which, thereby, promotes faster warming in the thermocline. At the same time, the overall cooling magnitude within the ML decreases compared to the period before 72-hour mark. This behavior indicates that the intensifying TC is now capable of pulling up warmer water from the BL, yet the vertical mixing has not penetrated deep enough to reach the cold water beneath the deepening IL. Consequently, the entrained warmer ocean

doi:10.6342/NTU202502292

water suppresses the typical SST-cooling effect, creating a more favorable environment for further TC intensification, as observed in group T28 and T29, as shown in Fig. 3.1a. In contrast, under the BLT00 configuration, increasing intensity of the TCs results in stronger induced vertical mixing (Fig. 4.1a). This enhanced mixing increases the SST-cooling effect significantly. The temperature profile below the IL also shows a progressively warming pattern as the IL deepens, reflecting the upward entrainment of colder water from the thermocline. In this scenario, the deepening ML signals the beginning of cold-water entrainment, resulting in more pronounced cooling than observed in the BLT30 cases. The BL acts as an insulating layer in the presence of warmer water while facilitating a stronger cooling signal when it is absent.

As the TCs intensify beyond the 96-hour mark reaching speed of 45-50 m s^{-1} in group T28, wind speed becomes sufficiently strong to drive vertical mixing that penetrates through the warm BL and extends into the colder water beneath the IL (Fig. 4.1b). This process is accompanied by a deepening of both the ML and the IL, which facilitates enhanced interactions between the base of the BL and the colder water at greater depths. In the BLT30 configuration, this deepening results in warming below the depth of the IL. Although the combination of air-sea heat loss and the entrainment of cold water further cools the ML, the warm water within the BL both weakens vertical mixing and mitigates the overall cooling effect compared to what is typically observed in BLT00. Conversely, in the BLT00 scenario (See Fig. 4.1a), the absence of a BL allows for a more pronounced cooling pattern within the ML, coupled with warming beneath it than in BLT30 due to more extensive entrainment of cold water from below the IL. ML and IL extend from 60 to below 90 meters contributing to the extensive cold entrainment, leading to a significant cooling exceeding 1˚C within the ML. Overall, this process produces a pronounced SST-cooling effect, as depicted in Fig. 3.2a. In comparison, these results show that the mixing

doi:10.6342/NTU202502292

of warmer water within the BL, combined with the limitation on the depth of induced vertical mixing, significantly reduces cooling within the ML. The SST-cooling effect is either mitigated or delayed, thereby influencing the TC intensification process.

In experiment SF05-LSW-VWS, a similar increasing warming signal within the BL is observed in BLT30 (Fig. 4.2b) compared to BLT00 (Fig. 4.2a). However, prior to the 120-hour mark, the weak intensity of the TCs results in minimal deepening of both the ML and IL, indicating that the induced vertical mixing is insufficient to penetrate the BL, which leaves it undisturbed (Fig. 4.2b). As a result, throughout the entire simulation, the warming pattern consistently appears within the BL. Consequently, the warm water contained in the BL remains isolated and is not entrained into the ML, leading to the enhanced cooling within the ML, particularly between 72 to 120 hours. These results provide an explanation for the relatively less SHF in the BLT30 configuration (Fig. 3.3b). On the other hand, the configuration BLT00 in SF05-LSW-VWS shows the typical cooling pattern in the ML and subsurface warming below the IL through vertical mixing (Fig. 4.2a). However, due to the relatively weak intensity, the magnitude of the ML cooling is less pronounced than that observed in SF02-LSW. Furthermore, the stronger warming pattern beneath the IL in BLT00 compared to BLT30 further illustrates the role of the BL to inhibit vertical mixing. The above results highlight the critical role of BLs in influencing ML thermodynamics in various TC phases. In the early phase of the TCs, the weak intensity yields weak vertical mixing that fails to penetrate the BL, resulting in a progressive warming within the BL and cooling within the ML. Conversely, once the cyclone intensifies sufficiently to entrain colder water from beneath the IL, the residual warmth retained within the BL serves to mitigate the cooling of the ML. This thermal moderation establishes a more conducive oceanic condition, ultimately favoring further TC intensification.

doi:10.6342/NTU202502292

4.2 Temperature change in the ocean column in fixed location

The previous section demonstrated the evolution of temperature in the ocean column following a TC passage, highlighting the key role of air–sea interactions. Furthermore, the ocean's dynamic response at a fixed location, including before, during, and after a TC, exerts varying influences on both the storm and its environment, especially in the presence of a BL. A thorough understanding of these processes is therefore vital for accurately predicting TC impacts on both oceanic and atmospheric systems. Figures 4.3 and 4.4 illustrate the temporal evolution of temperature along the ocean column at the location of TC passage at the 72-hour mark.

In the SF02-LSW simulation, before the 60-hour mark and in the absence of the BL (BLT00, see Fig. 4.3a), temperature anomalies within the ML near the surface remain minimal. Under calm weather conditions, solar heating creates a warm, thick ML with a well-defined thermocline; the positive temperature anomaly driven by shortwave radiation during the diurnal cycle is nearly offset by the cooling from weak wind-induced mechanical mixing, so that these two effects effectively cancel each other out, leaving the water column largely undisturbed.

As the system approaches the 72-hour mark, a negative anomaly emerges within the ML while a positive anomaly develops at and below its base. The intensifying winds associated with the approaching TC generate significant surface stress, which induces turbulent mixing in the upper ocean. This vigorous mixing deepens the ML and initiates vertical entrainment of colder thermocline water, causing the anomaly to intensify rapidly as the TC nears. This signal enlarges quicker as the TC approaches. Notably, the maximum positive anomaly, observed at the base of the ML due to steep temperature gradients, coincides with the onset of the TC's departure from the region. After the TC center passes, persistent wind stress continues to drive vertical mixing, ultimately

doi:10.6342/NTU202502292

resulting in substantial cooling within the ML. With a translation speed of approximately 2–3 m s^{-1}, Ekman pumping further entrains colder water without the restriction of the BL, thereby accentuating the cooling effect, leading to a pattern that is more pronounced when initial temperatures are higher under stronger TC intensities. Typically, once the TC departs, the ocean gradually restores its stratification, however, the recovery process can take several days to weeks, depending on the residual disturbances and subsequent weather conditions. In this study's quiescent oceanic setting, full recovery to the pre-storm state may require an even longer period.

In contrast, the BLT30 configuration exhibits a negative temperature anomaly within the deepening ML before the 72-hour mark (Fig. 4.3b), indicating more pronounced cooling compared to the BLT00 case. This difference is primarily attributed to the thinner ML, which cools more rapidly through enhanced air–sea heat loss and turbulent mixing induced by the weak TC. Additionally, a concomitant positive anomaly within the BL signifies a warming signal, which is corresponded with Fig. 4.1b. As the TC approaches, the ML deepens at an accelerated rate which is faster than that of the IL. The cooling at the 72-hour mark shows a larger cooling in magnitude than BLT00. This can be attributed to the weak intensity of TC. By comparing Fig. 4.3a with Fig. 4.3b, we observe that under weak intensity conditions, vertical mixing remains confined to the ML. In cases where a BL is present and the ML is comparatively thinner, mechanical mixing yields more pronounced cooling. Conversely, beyond the 72-hour mark, the stronger intensity drives vertical mixing that successfully entrains warm water from the BL, thereby suppressing the cooling effect within the ML.

For the SF05-LSW-VWS configuration, as the system approaches the 72-hour mark, the overall temperature patterns resemble those observed during the early stages of the SF02-LSW simulations (Fig. 4.4). In experiments T28 and T29, the ML exhibits more

doi:10.6342/NTU202502292

pronounced cooling in the BLT30 (Fig. 4.4b) configuration than in BLT00 (Fig. 4.4a). This difference can be attributed to the combined effects of a weaker TC intensity and thin ML, which yields a shallower maximum mixing depth, and a faster (albeit moderate) translation speed, which reduces the residence time of the TC over a given ocean region. Consequently, not only the vertical mixing has comfined within the ML but insufficient time to entrain appreciable warm water from the BL, leading to enhanced cooling, which corresponds with Figure 4.2b.

At the 96-hour mark, the ocean's response to a stronger storm intensity is evident (see Figs. 4.5 and 4.6). In the SF05-LSW-VWS simulation (Fig. 4.6), temperature changes remain nearly identical to those in Fig. 4.4 because the TC's weak intensity is insufficient to penetrate the BL. In the BLT00 configuration, a larger maximum positive temperature anomaly is observed at the interface between the ML and the thermocline after the TC's passage, suggesting that in the absence of BL hindrance, enhanced vertical mixing leads to ML cooling and subsurface warming (Fig. 4.6a). A similar positive anomaly is evident but weaker in the BLT30 configuration, indicating significant heat exchange between a warmed BL and the colder water below the IL (Fig. 4.6b). In contrast, the SF02-LSW simulation exhibits suppressed cooling within the ML as the TC approaches when a BL is present. This indicates that, at this stage, the TC's intensity is strong enough to promote vertical mixing that entrains warm water from the BL (see Fig. 4.5b). As a consequence, the cold wake left after the TC's passage is diminished, creating a condition that could favor further TC intensification or benefit subsequent storms traversing the area. Moreover, because the thermal structure remains largely intact thanks to the BL, we can expect the ocean's overall recovery time to be shortened, even though restoring the suppressed BL itself may be more challenging. Under identical intensity conditions, the BLT00 configuration shows a deeper ML base compared to the BLT30 case (see Fig.

doi:10.6342/NTU202502292

4.5a). Here, the rapid ML expansion entrains colder thermocline water, resulting in a greater temperature decrease that is particularly pronounced at higher initial temperatures during the TC passage (as observed in T29, not shown). After the passage, the continuous heat exchange with the thermocline further cools the ML reaching the magnitude around 1°C.

At the 120-hour mark (see Fig. 4.7), the SF02-LSW simulation reveals the entrainment of warm water from the BL prior to the TC's arrival between the 96-hour and 120-hour mark (Fig. 4.7b). During the TC passage, the ML deepens significantly by entraining cold water from the layers below. Interestingly, the most pronounced cooling signal occurs slightly after the 120-hour mark rather than just before it, despite the fact that the TC's periphery arrives ahead of its center. This observation suggests that vertical mixing induced by wind speed in the outer regions is insufficient to affect layers below the IL. In contrast, the combined effects of vertical mixing and Ekman pumping near the TC center can entrain cold water, although this process takes additional time due to the restraining influence of the BL, which eventually leads to the ML cooling. The magnitude of ML cooling is reduced compared to the BLT00 case (see Fig. 4.7a) because the earlier warm water entrainment counteracts some of the cooling effects. In turn, the suppressed cooling occurs at the end of the simulation in SF05-LSW-VWS, indicating that the TC eventually reaches a sufficient wind speed to break through the BL and entrain warm water upward (Fig. 4.8b). If the simulation period were extended, a more pronounced signal of suppressed cooling is likely to emerge. This extended duration would allow the delayed oceanic response to manifest more clearly, which has shown in SF02-LSW, offering deeper insights into the interplay between vertical mixing and the thermal structure during and after the TC passage.

doi:10.6342/NTU202502292

4.3 Temperature difference between experiment with different BL thickness

Sprintall and Tomczak (1992) provided compelling evidence for the existence of BLs in the surface layer of tropical oceans. In the WNP, where BL thickness ranges from 10 to 30 meters, these layers play a critical role in modulating ML thermodynamics. To further investigate the impact of varying BL thickness on ocean temperature variation, Figs. 4.9 and 4.10 illustrate the temperature differences observed as BL thickness increases relative to the BLT00 configuration. In SF02-LSW, as the thickness of the BLs increases, both the warming signal within the BL and the cooling signal within the ML emerge and intensify over time (Fig. 4.9). Prior to the first 72-hour mark, the thermal structure within the ML appears relatively cooler compared to the BLT00 configuration, and this cooling becomes more pronounced with thicker BLs. This signal further emphasizes that the TC is initially only able to mix the thinner ML before its wind stress becomes strong enough to penetrate the BL, resulting in more significant cooling in the ML.

After the initial cooling phase, a slight positive temperature anomaly emerges, not because induced vertical mixing reaches the BL, as noted in Fig. 4.9, but rather due to the more advanced cooling encountered in the BLT00 scenario. Moreover, the timing of when vertical mixing penetrates the warmed BL is delayed as the BL thickness increases, with the mixing occurring from around 72-hour (Fig. 4.9a) to 96-hour mark (Fig. 4.9c). This delay is evidenced by the emergence of relatively larger positive temperature anomalies at the onset of mixing. These anomalies arise from the difference between the enhanced cooling observed in the BLT00 configuration and the reduced cooling when a BL is present. Since the vertical mixing at this point is capable of entraining the warm ocean water up from the BL, the cooling signal within the ML has been suppressed. After

doi:10.6342/NTU202502292

the 96-hour mark, the pronounced positive anomaly indicates that the suppressed cooling effect becomes more significant with increasing BL thickness. This leads to a relative increase in the SHF uptake, contributing to a more favorable condition for TC intensification (Fig. 3.1a and 3.3a). Additionally, a negative anomaly is observable below and along the deepening IL in all BL thickness. This phenomenon is primarily attributed to the expansion of the ML in BLT00, which triggers an earlier onset of warming below the IL. The expanded ML accelerates the upward entrainment of colder water, leading to a contrast that results in a noticeable negative anomaly below the IL, setting it apart from scenarios with thicker BLs.

As in the SW05-LSW-VWS experiment, an increase in BL thickness leads to both a relative warming within the BL and enhanced cooling in the ML, similar to the early stage of SF02-LSW. Notably, the magnitude and duration of ML cooling are more pronounced here than in SF02-LSW, intensifying with increasing BL thickness and reaching up to 0.3˚C, as illustrated in Fig. 4.10. Due to the relatively weaker intensity over time, the induced vertical mixing in these cases cannot penetrate through the BL but is confined to the ML, resulting in amplified cooling. Moreover, increased BL thickness extends the duration of the cooling signal in the ML. Consequently, when TC is weak, a thicker BL has the ability to enlarge and prolong the SST-cooling effect, which results in a relatively lower SHF and creating unfavorable conditions for intensification, as depicted in Fig. 3.1b. Similar to the SF02-LSW simulation, a delayed and intensifying positive anomaly appears within the ML. This anomaly arises from cooling in the BLT00 configuration, rather than from warm-water entrainment.

In summary, our results demonstrate that the influence of the BLs on TC intensification depends critically on both the storm's intensity and the BL thickness, which is similar with the findings of Yan et al. 2017. This relationship can be

doi:10.6342/NTU202502292

distinguished into three phases. First, when TCs are so weak that the induced vertical mixing cannot reach the BLs, enhanced cooling in the ML creates unfavorable conditions for intensification. Second, when TCs are strong enough for vertical mixing to penetrate the BL but not below the IL, the cooling in the ML is suppressed due to the entrainment of the warm ocean water from the BL, thereby favoring further intensification with relatively higher temperature. Finally, when TCs are sufficiently strong to penetrate through the BLs and mix the cold water below the IL, the entrainment of the cooler water further cools the ML, however, the presence of warm water within the BL can still mitigate the overall cooling compared to cases without a BL. These results not only highlight the influence of the BLs on different TC intensity but also underscore the importance of accurately assessing the initial ocean thermal profiles, especially BL thickness, in order to improve forecasting accuracy.

4.4 Evolution of upper ocean heat content (UOHC)

The response of upper ocean temperature and heat content to TCs is primarily driven by the interplay between turbulence-induced mixing and vertical water movement (Zhang 2023). Chih and Wu (2020) have emphasized that high UOHC is an important factor for rapid intensification of TCs. Numerous studies have demonstrated a positive correlation between UOHC and TC intensification, underscoring the importance of accurately assessing the initial state of the ocean column prior to TC arrival.

The definition of UOHC is provided in Equation (4-1), where c_p denotes the specific heat capacity at constant pressure (4178 J kg^{-1} $°C^{-1}$ for seawater) and ρ represents the potential density of the ocean column. This formulation shows that higher initial temperatures lead to elevated UOHC values, with UOHC representing the vertically

doi:10.6342/NTU202502292

integrated thermal structure extending from the ocean surface to the depth of the 26°C isotherm.

$$UOHC = C_p \int_{Z_{T=26}}^{Z_T} \rho_i (T_i - 26) dz_i \quad (4\text{-}1)$$

From the fixed-location analysis, we can monitor the temporal evolution of the UOHC with and without the presence of the BL in the local ocean, capturing the actual UOHC evolution at that site, including pre-, during, and post-storm background variability. The corresponding UOHC in the fixed-location of 72-hour, 96-hour, and 120-hour mark is presented in Figs. 4.11-4.13.

In SF02-LSW configuration, as the storm approaches the 72-hour mark, the results show that before the arrival of the TC, UOHC under both BLT00 and BLT30 approximately remains essentially constant (Fig. 4.11a). Beyond the 72-hour mark, UOHC continues to exhibit only minor variation due to the weak intensity of TCs, showing the attendant conservation of energy within the upper ocean. Moreover, the BLT30 simulation persistently yields a slightly higher UOHC than BLT00, a difference attributable to the altered potential-density stratification in the upper ocean.

As the system approaches the 96-hour mark (Fig. 4.12a), UOHC remains essentially unchanged prior to TC arrival, reflecting energy conservation within the upper ocean. In the BLT30 configuration, however, a marked UOHC increase appears around the 96-hour mark, signifying enhanced upward entrainment of warm water into the mixed layer and deeper vertical mixing through the thickening isothermal layer. These processes diminish net ML cooling while warming waters beneath the IL. Following cyclone passage, UOHC declines sharply as cold thermocline water is entrained into the ML, evidencing that

doi:10.6342/NTU202502292

storm-induced mixing has become sufficiently intense to breach the BL. Additional, in the BLT30 configuration, where a pre-warmed barrier layer caps the mixed layer, the post-passage decline of UOHC exceeds that in BLT00. This larger UOHC decrement reflects a more efficient extraction of stored ocean heat and corresponds directly to an accelerated intensification rate in the presence of the BL.

In the SF02–LSW configuration at the 120-hour mark (Fig. 4.13a), similar to 96-hour fixed location analysis (Fig. 4.12a), UOHC remains essentially constant until TC arrival; during passage it exhibits a transient increase followed by a sharp decline. These features highlight the stabilizing influence from BL, which initially suppresses UOHC depletion under moderate forcing. By this stage, however, the intensified winds of TC overwhelm the BL's resistance, driving vigorous vertical mixing and cold-water entrainment into the ML. The resulting substantial reduction in upper-ocean heat content corresponds to an accelerated intensification rate facilitated by the presence of the BL.

In the SF05–LSW–VWS configuration, fixed-location analyses show that UOHC remains essentially constant throughout the simulation across all BL treatments (Figs. 4.11b, 4.12b, and 4.13b). This persistence reflects the cyclone's comparatively weak intensity and limited intensification rate relative to the SF02–LSW scenario. Moreover, the storm's moderate translation speed reduces its residence time over any given point, limiting the duration of wind-induced stress on the ocean surface. As a result, vertical mixing and cold-water entrainment into the mixed layer are minimal, and UOHC exhibits only negligible change during TC passage. A minor deviation is observed in group T28 and T29 at the 120-hour mark in the BLT00 run. By the end of the simulation, due to the stronger intensity, cold-water entrainment produces a slight decrease in UOHC under a moderate translation speed.

doi:10.6342/NTU202502292

In addition to fixed-location analyses, we also evaluate UOHC in a storm-following coordinate framework, recognizing that ocean–atmosphere feedbacks influence TCs intensity only in the storm's immediate vicinity. This Lagrangian approach typically reveals a larger net UOHC depletion during cyclone passage by sampling the ocean directly beneath the eyewall, thereby minimizing contamination from lateral heat advection and accurately capturing the instantaneous response of ocean thermal dynamics to air–sea interactions. The corresponding storm-following UOHC time series is presented in Figure 4.14.

In experiment SF02-LSW, the results show that TCs with thicker BLs can obtain higher UOHC than BLT00, as illustrated in Fig. 4.14a. Prior to 72 hours, the magnitude of UOHC steadily increases as the ML and IL deepen, accompanied by warming within the BL, where the difference is much clearer in higher temperature (see Fig. 4.1b). From the energy perspective, the gradual increase in UOHC suggests that heat is being stored in the BLs and gradually deepening of both ML and IL. Beyond the 96-hour mark, a drop in UOHC is observed, which suggests that the TC intensity at this point has reached an intensity sufficient to penetrate the BL and entrain colder water upward. This process effectively taps into the ocean's stored potential energy, facilitating further TC intensification. In contrast, the BLT00 configuration shows a mostly constant UOHC during the first 96 hours, with only a slight increase likely attributable to the deepening of the IL and ML as described in Eq. (2-3). Additionally, the comparison shows the timing of the UOHC drop is advanced in BLT00 compared to BLT30, indicating that vertical mixing, which entrains cold seawater upward from the thermocline, initiates earlier in the absence of a thicker BL (also evident in Fig. 4.1a). On the contrary, in SF05-LSW-VWS (Fig. 4.14b), the TC intensity is not sufficient to entrain warm water within the BL. The sighs of the deepening of both IL and ML are not significant owing to the weak vertical

doi:10.6342/NTU202502292

mixing. Furthermore, the enhanced cooling within the ML and warming within the BL nearly cancel each other out, therefore, resulting in relatively constant UOHC values in the BLT30 configuration across all temperature groups. The trend in BLT00 also shows similar behavior.

4.5 Evolution of equivalent upper ocean heat content (UOHCe)

To consider the stability of the ocean due to the presence of the salinity stratification, Shay et al. (2010) proposed a method for estimating the equivalent value of OHC, referred to as UOHCe, this variable has proven to be a more effective predictor of hurricane intensity changes than ocean heat content anomalies alone, especially during rapid intensification when considering ocean stability. The University of Miami had discussed the concept of the UOHCe by providing a detailed explanation of the derivation and discussing its significance across different ocean basins (see Eqs. (4-2) and (4-3)). Their analysis revealed that the stratification is much stronger in the Eastern Pacific where the Brunt-Väisälä frequency reaches a maximum (N_{max}) value of 24 cph, compared to the value of 6 to 12 cph observed in the Atlantic Ocean basin.

$$UOHCe = S \times C_p \int_{Z_{T=26}}^{Z_T} \rho_i (T_i - 26) dz_i \quad (4\text{-}2)$$

$$S = \sqrt{N_{max} / N_{ref}} \quad (4\text{-}3)$$

Figures 4.15-4.17 presents fixed-location UOHCe time series at 72-, 96-, and 120-hour mark and Fig. 4.18 presents the UOHCe results from each simulation following the TC center. Its definition is given in Eq. (4-2), where the parameter S is defined as the ratio

doi:10.6342/NTU202502292

of the maximum to the reference Brunt-Väisälä frequency, as illustrated in Eq. (4-3). This formulation enables an objective evaluation of the UOHC across ocean structures with varying stability, thereby emphasizing the influence of ocean stability in different basins and improving simulations coupling the ocean.

Despite parallels with total UOHC, the UOHCe follows a distinctly different trajectory, with a larger split between BLT00 and BLT30 driven by the enhanced stability imparted by the thicker BL in both fixed-location and storm-following analysis. For fixed-location analysis at the 72-hour mark in SF02-LSW configuration (Fig. 4.15a), both BLT00 and BLT30 simulations exhibit an upward trend in UOHCe as the cyclone approaches. In BLT00, this increase arises from two concurrent processes: ML deepening entrains modest amounts of colder thermocline water into the ML, while subsurface warming beneath the IL elevates temperatures where potential density is higher. By definition, these opposing thermal shifts produce a net rise in UOHCe prior to storm landfall. In BLT30, this increase can be attributed to the warming within the BL where high stability locates. Once the TC passes, UOHCe declines in both configurations, mirroring the post-passage decrease seen in total. The sharper contrast in UOHCe between BLT00 and BLT30 underscores how BL stratification modulates the balance of cooling and warming processes in the upper ocean.

At the 96-hour mark in SF02-LSW configuration (Fig. 4.16a), UOHCe in both BLT00 and BLT30 exhibits a clear upward trend as the TC approaches, with BLT30 values exceeding those of BLT00. In BLT00, UOHCe rises by roughly 10 W m^{-2} for group T28 and 20 W m^{-2} for group T29, driven by upper-ocean density increases and temperature increases below the IL through vertical mixing. In BLT30, corresponding increases of approximately 20 W m^{-2} (T28) and 50 W m^{-2} (T29) result from the combined

doi:10.6342/NTU202502292

effects of BL warming and heat redistribution, highlighting the dominant role of high stability and warming within the BL. During TC passage, UOHCe rises to a maximum then declines in both configurations as vertical mixing entrains colder thermocline water into the ML (Fig. 4.16a). Furthermore, the more pronounced post-passage decline in UOHCe under BLT30 reflects enhanced cold-water entrainment from the thermocline. The greater UOHCe reduction exhibited by ensemble members T28 and T29 in BLT30 is directly associated with their comparatively accelerated intensification rates relative to BLT00 (Fig. 3.1b)

At the 120-hour mark in SF02-LSW configuration, it reproduces the key features identified at 96 h, demonstrating an initial UOHCe buildup followed by a pronounced post-passage decline (Fig. 4.17a). Although the increase in UOHCe prior to the TC passage remains comparable in magnitude to that at 96 h, which reflects continued ML deepening and BL warming, the magnitude of the dissipation is amplified due to the stronger intensity during and after the passage of the TC. In the most intense ensemble member (T29), cold thermocline entrainment is so vigorous that UOHCe is effectively reduced to zero immediately after TC passage.

In the SF05–LSW–VWS configuration (Fig. 4.15b, 4.16b, and 4.17b), UOHCe exhibits a slight but consistent upward trend in both BLT00 and BLT30 throughout the majority of the integration, reflecting the insufficient intensity of the TCs to penetrate the gradually warming BL. Only at the 120-hour mark (Fig. 4.17b), the trend of BLT30 in group T28 shows a slight increase due to the upward warm-water entrainment from the BL. Moreover, the trends of the T29 in all fixed-loacation analysis show a comparatively significant increase during the TC passage due to the stronger intensity than the other simulations.

doi:10.6342/NTU202502292

For the storm-following cooridinate in experiment SF02-LSW (Fig. 4.18a), the increase in UOHCe over time follows a similar trend to that of the UOHC across both experiments during the first 96 hours, showing a gradual build-up. However, the difference between the BLT30 and BLT00 configurations is more pronounced in UOHCe. Specifically, while the maximum difference in UOHCe extends from 82.4 W m^{-2} to 112.0 W m^{-2} in BLT30, it ranges from only 50.7 W m^{-2} to 60.5 W m^{-2} in BLT00. This expansion underscores the increased warming within the BLs when they are thicker, highlighting how ocean stability influences the available potential energy stored above the 26°C isotherm as a critical reservoir that TCs can exploit for intensification. Compared with the result of UOHC (Fig. 4.14a), the BLT30 configuration exhibits an earlier onset of a gradual UOHCe increase, noticeable as early as the 24-hour mark. This early enhancement emphasizes that warming in the BL rapidly exceeds the cooling in the ML, a consequence of the larger stability within the BL during the first 96 hours. This trend demonstrates that the UOHCe is highly sensitive to variations in the BL. After 96 hours, UOHCe also shows a pronounced drop of a substantially larger magnitude than that seen in UOHC. This larger decline can be attributed to the deepening and eventual breakthrough of the BL, which allows strong vertical mixing induced by powerful TCs to entrain colder water into the ML. This mixing not only redistributes the heat but also alters the salinity, leading to an increase in salinity that suppresses ML cooling and reduces the maximum Brunt-Väisälä frequency while cooling the BL. Consequently, by definition, the UOHCe becomes lower than the initial ocean thermal structure and provides an explanation for the larger maximum difference in UOHCe compared to UOHC. In the BLT00 configuration, unlike the behavior seen in UOHC, the trend in UOHCe exhibits an increasing pattern. This divergence can be attributed to the Brunt-Väisälä frequency ratio (***S***). Specifically, the temperature below the IL decreases at a lapse

doi:10.6342/NTU202502292

rate of 0.1˚C m^{-1}, as illustrated in the 3DPWP setting in Fig. 2.2a, which leads to an increase in the Brunt-Väisälä frequency in the deeper layer (Fig. 2.2d). Consequently, the ratio of the Brunt-Väisälä frequency is greater than 1 (though it remains below 2), which amplifies the warming signal in UOHCe relative to UOHC. Furthermore, the larger drop in UOHCe observed after the 96-hour mark in BLT00 indicates that vertical mixing has successfully entrained cold seawater from the thermocline, leading to enhanced cooling in the ML.

Strangely, after the 120-hour mark following the storm center in SF02-LSW, both UOHC and UOHCe exhibit a rebound in value in both the BLT00 and BLT30 configurations. Under typical conditions, once UOHC decreases as a result of intense vertical mixing and cold-water entrainment, it is expected to remain low, unless the subsequent TC intensity lessens. However, in this case, ocean current analysis reveals a significant enhancement of the northerly current after 120 hours. This enhanced current advects warm water inward toward the TCs. When this warm water is averaged over the spatial domain where UOHC is evaluated, the effect of warm advection appears as a sudden increase in UOHC (and correspondingly in UOHCe). This discovery also provides an explanation of the rebound trend that has also appeared in SST change following the TCs, as shown in Fig. 3.2a. This observation reflects the important role of horizontal ocean dynamics, specifically, warm water advection by currents, in modulating the UOHC even when vertical processes would otherwise maintain depressed values.

As for SF05-LSW-VWS, the results similarly show a slight increase across all experiments, but this trend is more evident in UOHCe than in UOHC (Fig 4.18b). Lin et al. (2013) demonstrated that warm oceanic features, such as eddies with high UOHC, can limit storm-induced cooling and favor intensification, thereby contributing to improved

doi:10.6342/NTU202502292

TC intensity forecasting. Likewise, Chih and Wu (2020) emphasized that high UOHC plays a critical role in TC intensification, as evidenced by statistical analyses of their relationship. Although several studies have reported a positive correlation between high UOHC (or UOHCe) and TC intensification, the current results indicate that even as UOHCe increases, the intensification of TCs in both BLT00 and BLT30 in SF05-LSW-VWS remains slow. This observation is consistent with the definition of UOHCe, which implies that highly stratified water serves as a barrier to strong vertical mixing, a barrier that persists until vertical shear increases sufficiently to reduce the Richardson number below its critical threshold (Shay et al., 2010). As illustrated in Fig. 4.2b, the TCs in these experiments are too weak to initiate vertical mixing that penetrates through the BL, meaning that the heat energy stored within the BL and above the 26°C isotherm is not effectively harnessed for intensification. Therefore, these findings suggest that UOHCe may be less suitable as a parameter to explain TC intensification when the storms remain weak.

4.6 Heat budget analysis

The results from both SF02-LSW and SF05-LSW-VWS reveal clear warming signals in the subsurface ocean associated with the presence of BLs, as demonstrated in Figures 4.9 and 4.10. Warm water retained within the BL contributes to the intensification of TCs once it is effectively entrained through vertical mixing, thereby redistributing heat throughout the ocean column. Therefore, investigating ocean heat advection during TC evolution is essential for determining both the warming source within the BL and the magnitude of the SST-cooling effect. Figures 4.19 and 4.20 illustrate the heat budget

doi:10.6342/NTU202502292

following the TC passage in the BLT30, with the corresponding expression provided in Equation (4-4):

$$\frac{\partial H}{\partial t} = -u \cdot \nabla_h H - v \cdot \nabla_z H + Q_{rad} \quad (4\text{-}4)$$

In this expression, the terms from left to right represent horizontal heat advection, vertical heat advection, and the radiation term, which correspond to the top-to-bottom shadings shown in Figs 4.19 and 4.20. Here, the u- and v-components denote the ocean current, and H represents the heat content. The calculation of the net input radiation at a given depth is based on the Beer-Lambert Law, as shown in Eq. (4-5):

$$Q_{rad}(z) = I_0 e^{-\kappa z} \quad (4\text{-}5)$$

In this equation, $\boldsymbol{Z}$ represents the depth in the ocean, $\boldsymbol{I_0}$ denotes the intensity of the shortwave radiation at the surface, $\boldsymbol{\kappa}$ is the attenuation coefficient. The typical value of $\boldsymbol{\kappa}$ in varies depending on water clarity and the presence of particles or dissolved substances. If the ocean water contains more presence of particles or dissolved substances in the ocean. In coastal or turbid waters that have high concentrations of suspended particles and organic matter, the attenuation coefficient can range from 0.1 to 1.0 m^{-1}, or even higher. In contrast, for clear oceanic waters, $\boldsymbol{\kappa}$ is typically within the range of 0.04 to 0.06 m^{-1}. In this study, $\boldsymbol{\kappa}$ is set to 0.05 m^{-1} in these simulations to represent typical clear oceanic conditions.

In the SF02-LSW experiment, during the first 72 hours when TC intensity is relatively weak, Fig. 4.19 shows only slight signals of both horizontal and vertical advection. Notably, the magnitude of vertical advection gradually increases at depths below the IL, indicating that the heat exchange between the warmed BL and the

doi:10.6342/NTU202502292

underlying thermocline. This entrainment results in a warming of the subsurface, as the process transfers the accumulated heat from the BL downward. The warm advection beneath the IL leads to the positive temperature change, a finding that is consistent with the thermal anomalies depicted in Fig. 4.1b. After the 96-hour mark, when TCs intensifies to the point where it can mix the entire ocean column, both horizontal and vertical advection exhibit negative values. At this stage, the induced vertical mixing has effectively penetrated the BLs, entraining not only the warm water stored within the BL but also incorporating the colder water from the deeper layers. This vigorous mixing results in overall cold advection across the whole ocean column resulting in a negative vertical advection in Fig. 4.19. In the analysis of the radiation term, a distinct diurnal cycle is evident, with the radiation intensity decreasing with depth. In the BLT30, where the ML extends to approximately 16 meters, the downward shortwave radiation reaches the BL. Given the high stability of the BL, external perturbations are minimal, allowing the absorbed shortwave radiation to effectively warm and be retained within this layer. Over time, the accumulated energy in the BL contributes to a progressive warming until the onset of vertical mixing, induced by intensifying TCs, disrupts this stored heat.

In the SF05-LSW-VWS scenario (Fig. 4.20), TCs remain too weak to drive vertical mixing that penetrates through the BL, as further evidenced in Fig. 4.2b. Therefore, horizontal advection remains weak and vertical advection shows only a gradual increase below the IL, resembling the pattern observed in the SF02-LSW experiment prior to the 96-hour mark. Since the cold water in the thermocline has not entrained upward, there is no pronounced negative value in either advection component. Additionally, the radiation term follows a similar pattern to that seen in SF02-LSW: downward shortwave radiation penetrates the BL, where its absorption leads to warming that is effectively preserved in the BL. However, in this scenario, the preserved energy remains unused due to the

doi:10.6342/NTU202502292

insufficient intensity to drive the vertical mixing. In summary, this study reveals that the observed warming within the BL is primarily driven by the influx of shortwave radiation coupled with a stabilization of the oceanic column. When TC intensity remains weak, a comprehensive heat budget analysis reveals that both horizontal and vertical heat advection contribute only marginally to the heat exchange. In contrast, as the TC intensifies, negative vertical heat advection emerges as the dominant factor, primarily through the entrainment of colder water from deeper layers, which ultimately alters the thermodynamic properties of the ML.

In this idealized simulation, the setting of the initial ocean is configured without any preset currents and with a periodic boundary condition. Even though the BL possesses high resistance to vertical mixing owing to its high stability, which leads to the energy accumulation. The formation and sustained presence of the BL in natural settings may still be influenced by horizontal currents at various depths. BLs have the capacity to absorb shortwave radiation, generating a warming signal as a result of energy preservation. Ultimately, this warming mechanism may influence the intensification of TCs, highlighting the critical need for a thorough investigation of the initial ocean structure to improve future TC forecasting.

doi:10.6342/NTU202502292

Chapter 5

Conclusions

5.1 Discussions

In this study, the initial ocean structure is characterized with a constant depth of the IL about 46.4 meters, with a lapse rate of 0.1˚C m^{-1} below. As the definition of the BL thickness, the difference between the ML and the IL, this setup naturally results in a thinner ML alongside a thicker BL, as shown in Fig. 2.2. Therefore, for a TC to utilize the warm water stored in the BL, it must intensify enough to reach the top of the BL. Similarly, TCs must continue strengthening until they can break through the BL into the thermocline, which then triggers cooling in the ML. The relationship between TC intensity and ML cooling, which helps define these intensity thresholds, is further examined and presented in Fig. 5.1.

Figure 5.1a shows the scatter plot between TC intensity and the ML cooling in the SF02-LSW experiment. For wind speed below roughly 30 m s^{-1}, a greater ML cooling is observed in the BLT30 configuration compared to BLT00, implying that vertical mixing is largely confined to the ML at these lower intensities (with T27 excluded due to its low intensity). When the wind stress reaches about 40 m s^{-1}, the rate of ML temperature decrease accelerates in BLT00, suggesting that vertical mixing has begun to penetrate into the thermocline and entrain colder water upward, resulting in a more pronounced cooling. In contrast, the ML cooling in BLT30 remains near 0.3˚C, which indicates the moderating influence of the BL through the entrainment of warmer water and a restriction on deeper vertical mixing. As the intensity increases beyond 50 m s^{-1}, both configurations exhibit further cooling; however, in the T29 group, the temperature

doi:10.6342/NTU202502292

drop in BLT00 exceeds 2˚C, while in BLT30 it is suppressed to roughly 1˚C, which are corresponding with Fig. 4.1. This crossover in cooling behavior underscores how the presence of the BL can both limit vertical mixing and preserve warm water, thereby influencing the extent of ML cooling.

In SF05-LSW-VWS, a similar “cross” between BLT00 and BLT30 is observed, as shown in Fig. 5.1b, though the criteria for this transition are shifted to slightly higher intensities compared to SF02-LSW. Analysis of the temperature trends, excluding the T27 case, reveals that both BLT00 and BLT30 exhibit a clear cooling signal throughout the evolution of TCs. Notably, the cooling in the ML is more pronounced in BLT30 compared to BLT00, as illustrated in Fig. 4.2. This behavior is attributed to the thinner ML in BLT30, where vertical mixing is confined to a narrower depth range, resulting in greater heat loss and a more significant drop in ML temperature before the entrainment of warm water occurs. Therefore, under the same weak intensity conditions, this finding suggests that the presence of the BL enhances the temperature reduction in the ML, as seen in the early stage of the SF02-LSW. Prior to reaching a wind speed of 40 m s^{-1}, the ML in BLT00 undergoes only a modest temperature decrease, which is smaller than the approximately 0.2˚C cooling observed in BLT30. As TCs intensify to approximately 40 m s^{-1}, the temperature trends for BLT00 and BLT30 converge, marking a crossing point between the two configurations. Notably, when the intensity in T29 reaches about 50 m s^{-1}, an accelerated temperature drop is evident in BLT00, whereas the cooling in BLT30 remains consistently near 0.2˚C (BLT30 in T28 cannot reach to 50 m s^{-1}). Additionally, the higher threshold for significant ML cooling in BLT00 can be attributed to the faster translation speed of TCs in this scenario, compared to SF02-LSW. These observations suggest that the presence of the BL not only amplifies the cooling in the ML but also sustains it over time, which is likely due to the lack of residence time. This

doi:10.6342/NTU202502292

prolonged cooling limits the vertical mixing process, hampering the entrainment of warm water from the BL to feedback on the TCs, and thereby exerts a cooling signal in the ML which is unfavorable for storm intensification.

By comparing the BLT00 and BLT30 experiments in the SF02-LSW (Fig. 5.1a) configuration, we determine that the threshold for TCs to effectively entrain the ocean layers depends on the presence of the BL and TC intensity. When the BL is absent (BLT00), the IL can be reached by induced vertical mixing at the maximum wind speeds of approximately 40 m s^{-1}. However, with the presence of the BL (BLT30), TCs must exceed wind speeds of 50 m s^{-1} to achieve the same level of entrainment. This finding underscores the significant role of salinity stratification in enhancing the stability of the ocean column, acting as a "barrier" that limits vertical mixing and demands a higher TC intensity to entrain the underlying cold water. Furthermore, the differences observed in ML temperature variations between BLT00 and BLT30 are consistent with the results of Yan et al. (2017), highlighting how the BL modulates ML temperature across different TC intensities. Besides, under unfavorable environmental conditions with moderate translation speed as shown in SF05-LSW-VWS (Fig. 5.1b), TCs have to take longer to meet the higher criteria than in SF02-LSW to penetrate the IL due to the lack of the residence time. BL acts as a negative contributor under weak TC intensity by enhancing the cooling effect, which is similar to the early stage of TCs in SF02-LSW.

Figure 5.2a illustrates the scatter plot between TC intensity and alterations in the UOHCe under the SF02-LSW configuration. As TCs intensify, enhanced vertical mixing deepens the ML until the cold water in the thermocline is entrained, resulting in a significant temperature drop (as shown in Fig. 5.1a) and, consequently, leading to the negative feedback on intensification. This reduction in UOHCe thus serves as an indicator for quantifying the minimum TC intensity needed to access the cold water below the IL.

doi:10.6342/NTU202502292

In the BLT30 configuration, UOHC (and its effective counterpart, UOHCe) increases noticeably during the early stages when TC intensity is below 40 m s^{-1}, but falls to negative values once the intensity exceeds about 50 m s^{-1}, indicating that the thermocline has been penetrated. This behavior also implies that both the threshold and timing for BLT30 to encounter the IL are higher and more delayed than in BLT00, demonstrating the role of the BL in restricting vertical mixing. Additionally, in the SF05-LSW-VWS scenario, the gradual increasing trends are shown in Fig. 5.2b, due to the overall weaker TC intensities and the modest deepening of both the ML and IL. Although the UOHC dynamics exhibit similarities to the ML temperature changes shown in Fig. 5.1b, the latter appears to be a more direct indicator of both the magnitude and timing required to disrupt the BL and the IL.

5.2 Conclusions

Investigating the effects of BLs with varying thicknesses on TC intensity is crucial for understanding changes in ocean structure and the subsequent air-sea interaction during a TC's passage. Cooling within the ML is mainly attributed to the induced vertical mixing and the associated heat flux. However, with the presence of the BLs, its high stability restricts vertical motion and thereby TCs must reach greater intensity to penetrate the BLs to entrain the colder water below the IL. As the TC intensifies, both the depth of the ML and IL deepen.

This study has analyzed the influence of BLs on TCs at different stages of development. Under favorable environmental conditions, which is characterized by higher shortwave radiation input, reduced wind shear, and moderate or fast translation speed, TC intensification is enhanced, diminishing the relative impact of the BLs.

doi:10.6342/NTU202502292

Conversely, in environments with unfavorable conditions and lower initial SST, the presence of a BL leads to a slower intensification rate, thereby providing negative feedback on TC intensification. Notably, under very strong TC intensity, the presence of the BL contributes to a greater intensification rate by helping to preserve and eventually release stored heat. Therefore, contrary to some previous studies suggesting that BL feedback invariably promotes TC intensification (Balaguru et al. 2012; Hlywiak and Nolan 2019), our simulation results indicate that the effects of BLs are contingent upon the current TC intensity and environmental conditions. This nuanced understanding emphasizes the importance of thoroughly investigating the initial ocean structure for improving future TC forecasting.

In our investigation of the BLs, we observe that their presence can suppress SST cooling in a manner consistent with previous research. In SF02-LSW, the high stability of the BL inhibits vertical mixing, showing the effectiveness of blocking the induced vertical mixing from the high ocean stability and resulting in less cooling of the ML during the later stages compared to cases without BLs. As vertical mixing eventually reaches the BL, a warming signal emerges due to the accumulated heat, which then helps to suppress further ML cooling. Notably, in the wind speed reaches the range of 40 to 50 m s^{-1}, TCs are strong enough to penetrate the BL but not enough for the IL, allowing warm water stored in the BL to mix into the ML. This process delays the cooling effect even when cold water from the thermocline eventually contributes to ML cooling, thereby creating conditions that are more favorable for TC intensification.

Conversely, when TCs are weak, typically under 40 m s^{-1} as observed in SF05-LSW-VWS and the early stage in SF02-LSW, the vertical mixing is too restricted by the BL to reach the deeper layers. This leads to enhanced and prolonged cooling within the relatively thin ML, generating an unfavorable ocean condition for TC intensification.

doi:10.6342/NTU202502292

These findings demonstrate that the influence of BLs on TC development is intensity-dependent, aligning with the observations reported by Yan et al. (2017). Moreover, our results reveal that this intensity-dependent BL effect can produce qualitatively different responses throughout the TC lifecycle via two-way ocean–atmosphere interactions, thereby modulating the rate of intensification at each developmental stage. Specifically, this finding further highlight that the presence of BLs not only alters ML thermodynamics by regulating wind-induced vertical mixing as wind speed increases, but also influences TC intensity by modifying surface heat fluxes and temperature within the ML, thus shaping the cyclone's intensification dynamics.

In addition to the enhanced cooling observed in the ML under weak TC intensity, the occurrence of the warming signal within the BLs is largely attributed to the absorption of shortwave radiation. According to the equation of the heat budget, the contributions from both horizontal and vertical advection are minimal during the early stages of TC development when a BL is present. At this early stage, a portion of the shortwave radiation penetrates the ocean's surface layers and reaches the BL. Due to the high stability inherent to the BL, this energy is efficiently preserved, leading to a warming signal within that layer. As the TC intensifies, vertical advection becomes the dominant process, driving more vigorous mixing within the ocean column. This enhanced vertical mixing entrains the warm water from the BL along with the colder water from below the IL. In other words, once the TC reaches a critical intensity, the previously preserved energy in the BL is partially redistributed. As the TC further intensifies, cold vertical advection leads to the cooling within the ML through the entrainment from the thermocline. These findings are consistent with earlier research (Price, 1981), which also highlighted the mixing-dominated cooling as a function of TC intensity. Therefore, the preserved energy in the BL can serve as a potential heat source

doi:10.6342/NTU202502292

for intensification under favorable conditions, yet its potential is only realized when the TC is strong enough to overcome the stabilizing influence of the BL.

In terms of UOHC, the results indicate that higher UOHC can lead to a greater intensification rate for strongly forced TCs, emphasizing the critical role of the initial ocean thermal structure (Lin et al., 2013). As TCs intensify, the presence of a BL causes UOHC to gradually increase up until the point where mixing brings cold water from the thermocline upward. Here, the warming in the BL, combined with the deepening of both the ML and the IL, produces a higher overall UOHC compared to situations without BLs. A subsequent drop in UOHC then signals the onset of deep vertical mixing that entrains cold water below the IL.

Moreover, when examining the UOHCe, the results reveal a larger quantitative difference in the presence of BLs, underscoring the influence of salinity stratification. In the SF05-LSW-VWS scenario, UOHCe appears to better capture the effect of the BLs; however, it is less applicable for weak TCs that are unable to fully exploit the available UOHCe. Nonetheless, once TCs exceed a certain intensity threshold, UOHCe becomes a useful indicator of intensification.

5.3 Future works

Future work to refine our understanding of the ocean–TC interaction can be conducted by incorporating a more realistic representation of the ocean's thermal structure. In this study, we emphasize the significance of the initial ocean structure prior to a TC passage and investigated how BLs influence TC evolution. However, our experiments assume a constant depth for the IL, whereas De Boyer Montégut et al. (2004) demonstrated that both BL thickness and ML depth vary across different ocean basins. In

doi:10.6342/NTU202502292

addition, several studies have shown that TCs are more likely to intensify when traversing thicker, warmer MLs (Zhang et al., 2024).

Even when BL thickness remains fixed, variations in the initial depth of the IL (or ML) may significantly modify the BL's impact on TC intensity. Theoretically, a thicker ML elevates the bar that vertical mixing must overcome to reach the BL and the underlying thermocline. This concept is supported by the principles of Ekman pumping, suggesting that, in warm and thick ML conditions, a higher UOHC is available to fuel TC intensification. Conversely, energy accumulation in the BL might decrease due to the dissipation of shortwave radiation, potentially reducing the warming signal within the BL and the suppression of SST cooling observed in this study. Therefore, conducting additional simulations that vary the ML depth while keeping the BL thickness constant is essential and would provide more accurate insights into the influence of BLs on TC intensity and help define the thresholds required for vertical mixing to reach the thermocline. Ultimately, these efforts underscore the importance of better characterizing the pre-TC ocean structure in improving TC intensity forecasting.

Additionally, our study reveals that the influence of the BL on TC evolution strongly depends on the cyclone's current intensity. In particular, when a TC is robust, the presence of the BL appears to suppress the cooling effect of the SST and within the ML, thereby establishing conditions conducive to further intensification. However, several factors require careful consideration when appling to the reality. These include variations in ocean currents, differences in regional ocean depths, and additional freshwater inputs, such as those from river plumes and local precipitation, all of which could modulate the formation and the impact of the BL on TC intensity. Consequently, a comprehensive analysis of historical storms is essential for fully elucidating the role of the BL in TC evolution. To bridge the gap between idealized experiments and the complex reality of

doi:10.6342/NTU202502292

TC–ocean interactions, future studies might incorporate case studies of historical storms to benchmark and evaluate the modeled interaction between BL and TCs to not only refine the theoretical framework in this study but also calibrate model parameters and settings for improving forcast accuracy. Therefore, investigating these dimensions in the future research will not only refine our understanding of the underlying dynamics but also enhance predictive capabilities for future TC behavior.

doi:10.6342/NTU202502292

References

Balaguru, K., P. Chang, R. Saravanan, L. R. Leung, Z. Xu, M. Li, and J. S. Hsieh, 2012: Ocean barrier layers' effect on tropical cyclone intensification. *Proc. Natl. Acad. Sci. U.S.A.*, **109**, 14343–14347. https://doi.org/10.1073/pnas.1201364109

Bhatia, K., G. Vecchi, H. Murakami, S. Underwood, and J. Kossin, 2018: Projected response of tropical cyclone intensity and intensification in a global climate model. *J. Climate*, **31**, 8281–8303, https://doi.org/10.1175/JCLI-D-17-0898.1.

Chandra, A., and S. Kumar, 2021: Sea surface temperature and ocean heat content during tropical cyclones Pam (2015) and Winston (2016) in the Southwest Pacific region. *Mon. Wea. Rev.*, **149**, 1173–1187.

Chang, K.-F., C.-C. Wu, and K. Ito, 2023: On the rapid weakening of Typhoon Trami (2018): Strong sea surface temperature cooling associated with slow translation speed. *Mon. Wea. Rev.*, **151**, 227–251. https://doi.org/10.1175/MWR-D-22-0039.1

Chih, C.-H., and C.-C. Wu, 2020: Exploratory analysis of upper-ocean heat content and sea surface temperature underlying tropical cyclone rapid intensification in the western North Pacific. *J. Climate*, **33**, 1031–1050. https://doi.org/10.1175/JCLI-D-19-0305.1

Chu, P. C., and C. Fan, 2023: Global climatological data of ocean thermohaline parameters derived from WOA18. *Sci. Data*, **10**, Article 408. https://doi.org/10.25921/j3v2-jy50

De Boyer Montégut, C., G. Madec, A. S. Fischer, A. Lazar, and D. Iudicone, 2004: Mixed layer depth over the global ocean: An examination of profile data and a profile-based climatology. *J. Geophys. Res.*, **109**, C12003. https://doi.org/10.1029/2004JC002378

doi:10.6342/NTU202502292

Emanuel, K. A., 1986: An air-sea interaction theory for tropical cyclones. Part I: Steady-state maintenance. *J. Atmos. Sci.*, **43**, 585–605. https://doi.org/10.1175/1520-0469(1986)043<0585:AASITF>2.0.CO;2

Feng, X. 2024. Translation speed slowdown and poleward migration of western North Pacific tropical cyclones. *npj Clim. Atmos. Sci.* **7**:196. https://doi.org/10.1038/s41612-024-00748-5

Garratt, J. R., 1977: Review of Drag Coefficients over Oceans and Continents. *Mon. Wea. Rev.*, **105**, 915–929, https://doi.org/10.1175/1520-0493(1977)105<0915:RODCOO>2.0.CO;2.

George, J. V., P. N. Vinayachandran, V. Vijith, V. Thushara, A. A. Nayak, S. M. Pargaonkar, P. Amol, K. Vijaykumar, and A. J. Matthews. 2019. Mechanisms of barrier layer formation and erosion from in situ observations in the Bay of Bengal. *J. Phys. Oceanogr.* **49**(5):1183–1200. https://doi.org/10.1175/JPO-D-18-0204.1.

Guo, X., J. P. Kossin, and Z.-M. Tan, 2024: The co-variability of SST and vertical wind shear on the variability of tropical cyclone intensity change in the Northern Hemisphere. *Climate Dyn.*, **62**, 2581–2594. https://doi.org/10.1007/s00382-023-07049-2

Hlywiak, J., and D. S. Nolan, 2019: The influence of oceanic barrier layers on tropical cyclone intensity as determined through idealized, coupled numerical simulations. *J. Phys. Oceanogr.*, **49**, 1723–1745. https://doi.org/10.1175/JPO-D-18-0267.1

Kara, A. B., P. A. Rochford, and H. E. Hurlburt, 2000: Mixed layer depth variability and barrier layer formation over the North Pacific Ocean. *J. Geophys. Res.: Oceans*, **105**, 16783–16801. https://doi.org/10.1029/2000JC900071

Leroux, M.-D., M. Plu, D. Barbary, F. Roux, and P. Arbogast, 2013: Dynamical and physical processes leading to tropical cyclone intensification under upper-level

doi:10.6342/NTU202502292

trough forcing. *J. Atmos. Sci.*, **70**, 2547–2565, https://doi.org/10.1175/JAS-D-12-0293.1

Li, G., Zhang, Y., Xiao, J., Song, X., Abraham, J., Cheng, L., & Zhu, J. (2019). Examining the salinity change in the upper Pacific Ocean during the Argo period. *Climate Dynamics, 53*(11-12), 6055-6074. https://doi.org/10.1007/s00382-019-04912-z

Lin, I.-I., W.-T. Liu, C.-C. Wu, G.-T. F. Wong, C. Hu, Z. Chen, W.-D. Liang, Y. Yang, and K.-K. Liu, 2003: New evidence for enhanced ocean primary production triggered by a tropical cyclone. *Geophys. Res. Lett.*, **30**, 1718. https://doi.org/10.1029/2003GL017141

——, G.-J. Goni, J.-A. Knaff, C. Forbes, and M.-M. Ali, 2013: Ocean heat content for tropical cyclone intensity forecasting and its impact on storm surge. *Natural Hazards*, **66**, 1481–1500. https://doi.org/10.1007/s11069-012-0214-5

Lukas, R., and E. Lindstrom, 1991: The mixed layer of the western equatorial Pacific Ocean. *J. Geophys. Res.: Oceans*, **96**, 3343–3357. https://doi.org/10.1029/90JC01957

McTaggart-Cowan, R., L. F. Bosart, J. R. Gyakum, and E. H. Atallah. 2007. Hurricane Katrina (2005). Part I: Complex life cycle of an intense tropical cyclone. Mon. Wea. Rev. 135(12):3905–3926. https://doi.org/10.1175/2007MWR1875.1.

Price, J. F., 1981: Upper ocean response to a hurricane. *J. Phys. Oceanogr.*, **11**, 153–175. https://doi.org/10.1175/1520-0485(1981)011<0153:UORTAH>2.0.CO;2

——, 1984: The oceanic response to a hurricane. *J. Phys. Oceanogr.*, **14**, 949–970.

——, T.-B. Sanford, and G.-Z. Forristall, 1994: Forced stage response to a moving hurricane. *J. Phys. Oceanogr.*, **24**, 233–260. https://doi.org/10.1175/1520-0485(1994)024<0233:FSRTAM>2.0.CO;2

doi:10.6342/NTU202502292

Reul, N., Quilfen, Y., Chapron, B., Fournier, S., Kudryavtsev, V., and Sabia, R., 2014: Multisensor observations of the Amazon-Orinoco river plume interactions with hurricanes. *J. Geophys. Res. Oceans*, **119**, 8271–8295, https://doi.org/10.1002/2014JC010107

Rios-Berrios, R., and R.-D. Torn, 2017: Climatological analysis of tropical cyclone intensity changes under moderate vertical wind shear. *Mon. Wea. Rev.*, **145**, 1717–1738. https://doi.org/10.1175/MWR-D-16-0350.1

——, P. M. Finocchio, J. J. Alland, X. Chen, M. S. Fischer, S. N. Stevenson, and D. Tao. 2024. A review of the interactions between tropical cyclones and environmental vertical wind shear. J. Atmos. Sci. 81(4):713–741. https://doi.org/10.1175/JAS-D-23-0022.1

Shay, L. K., R. L. Elsberry, and P. G. Black. 1989. Vertical structure of the ocean current response to a hurricane. J. Phys. Oceanogr. 19(5):649–669. https://doi.org/10.1175/1520-0485(1989)019<0649:VSOTOC>2.0.CO;2

——, and J.-K. Brewster, 2010: Oceanic heat content variability in the eastern Pacific Ocean for hurricane intensity forecasting. *Mon. Wea. Rev.*, **138**, 2110–2125. https://doi.org/10.1175/2010MWR3189.1

Sprintall, J., and M. Tomczak, 1992: Evidence of the barrier layer in the surface layer of the tropics. *J. Geophys. Res.*, **97**, 7305–7316.

Stewart, R. H. (2004), Introduction to physical oceanography, Department of Oceanography, Texas A & M University. https://oaktrust.library.tamu.edu/items/254c2944-dc14-445e-adde-663c63b4cc2e

Tao, D., and F. Zhang, 2019: Evolution of dynamic and thermodynamic structures before and during rapid intensification of tropical cyclones: Sensitivity to vertical wind

doi:10.6342/NTU202502292

shear. *Mon. Wea. Rev.*, **147**, 1171–1191, https://doi.org/10.1175/MWR-D-18-0173.1.

Vialard, J., and Delecluse, P., 1998: An OGCM Study for the TOGA Decade. Part II: Barrier-Layer Formation and Variability. *J. Phys. Oceanogr.*, **28**, 1089–1106, https://doi.org/10.1175/1520-0485(1998)028<1089:AOSFTT>2.0.CO;2

Vincent, E. M., M. Lengaigne, J. Vialard, G. Madec, N. C. Jourdain, and S. Masson, 2012: Assessing the oceanic control on the amplitude of sea surface cooling induced by tropical cyclones. *J. Geophys. Res.*, **117**, C05023, https://doi.org/10.1029/2011JC007705

Wang, G., B. Zhao, F. Qiao, and C. Zhao. 2018. Rapid intensification of Super Typhoon Haiyan: The important role of a warm-core ocean eddy. Ocean Dyn. 68:1649–1661. https://doi.org/10.1007/s10236-018-1217-x.

Wei, J., Liu, X., and Jiang, G., 2018: Parameterizing sea surface temperature cooling induced by tropical cyclones using a multivariate linear regression model. *Acta Oceanologica Sinica*, **37**, 1–10, https://doi.org/10.1007/s13131-018-1153-0

Wu, C.-C., C.-Y. Lee, and I.-I. Lin, 2007: The effect of the ocean eddy on tropical cyclone intensity. *J. Atmos. Sci.*, **64**, 3562–3578. https://doi.org/10.1175/JAS4051.1

——, W.-T. Tu, I.-F. Pun, I.-I. Lin, and M.-S. Peng, 2016: Tropical cyclone-ocean interaction in Typhoon Megi (2010)—A synergy study based on ITOP observations and atmosphere-ocean coupled model simulations. *J. Geophys. Res.: Atmos.*, **121**, 153–167. https://doi.org/10.1002/2015JD024198

Xu, J., and Y. Wang, 2018: Dependence of tropical cyclone intensification rate on sea surface temperature, storm intensity, and size in the western North Pacific. *Wea. Forecasting*, **33**, 523–537, https://doi.org/10.1175/WAF-D-17-0095.1.

doi:10.6342/NTU202502292

Yablonsky, R. M., and I. Ginis, 2013: Impact of a warm ocean eddy's circulation on hurricane-induced sea surface cooling with implications for hurricane intensity. *Mon. Wea. Rev.*, **141**, 997–1021, https://doi.org/10.1175/MWR-D-12-00248.1.

Yan, Y., L. Li, and C. Wang, 2017: The effects of oceanic barrier layer on the upper ocean response to tropical cyclones. *J. Geophys. Res.: Oceans*, **122**, 4567–4584. https://doi.org/10.1002/2017JC012694

You, Y. 1998. Rain-formed barrier layer of the western equatorial Pacific warm pool: A case study. *J. Geophys. Res. Oceans* **103**(C3):5361–5378. https://doi.org/10.1029/97JC03421.

Zhang, H., 2023: Modulation of upper ocean vertical temperature structure and heat content by a fast-moving tropical cyclone. *J. Phys. Oceanogr.*, **53**, 493–508.

Zhang, Y., Han, K., Sun, Y., Lin, Y., Zhai, P., Guo, X., and Zhong, W. (2024). Impact of ocean mixed layer depth on tropical cyclone characteristics: A numerical investigation. *Front. Mar. Sci.* **11**, 1395492. https://doi.org/10.3389/fmars.2024.1395492

doi:10.6342/NTU202502292

Tables

Table 2.1 Experimental designs of the sensitivity experiments. Numbers in the names of experiments indicate the speed of uniformed steering flow (SF). Vertical wind shear (VWS) is defined as the wind speed difference between 200 hPa and 850 hPa.

Experiments	Translation speed	Additional features descriptions
SF02	2~3	
SF02-LSW	2~3	1. Lower shortwave radiation
SF02-LSW-VWS	2~3	1. Lower shortwave radiation 2. Adding VWS
SF05	5~6	
SF05-LSW	5~6	1. Lower shortwave radiation
SF05-LSW-VWS	5~7	1. Lower shortwave radiation 2. Adding VWS

doi:10.6342/NTU202502292

Figures

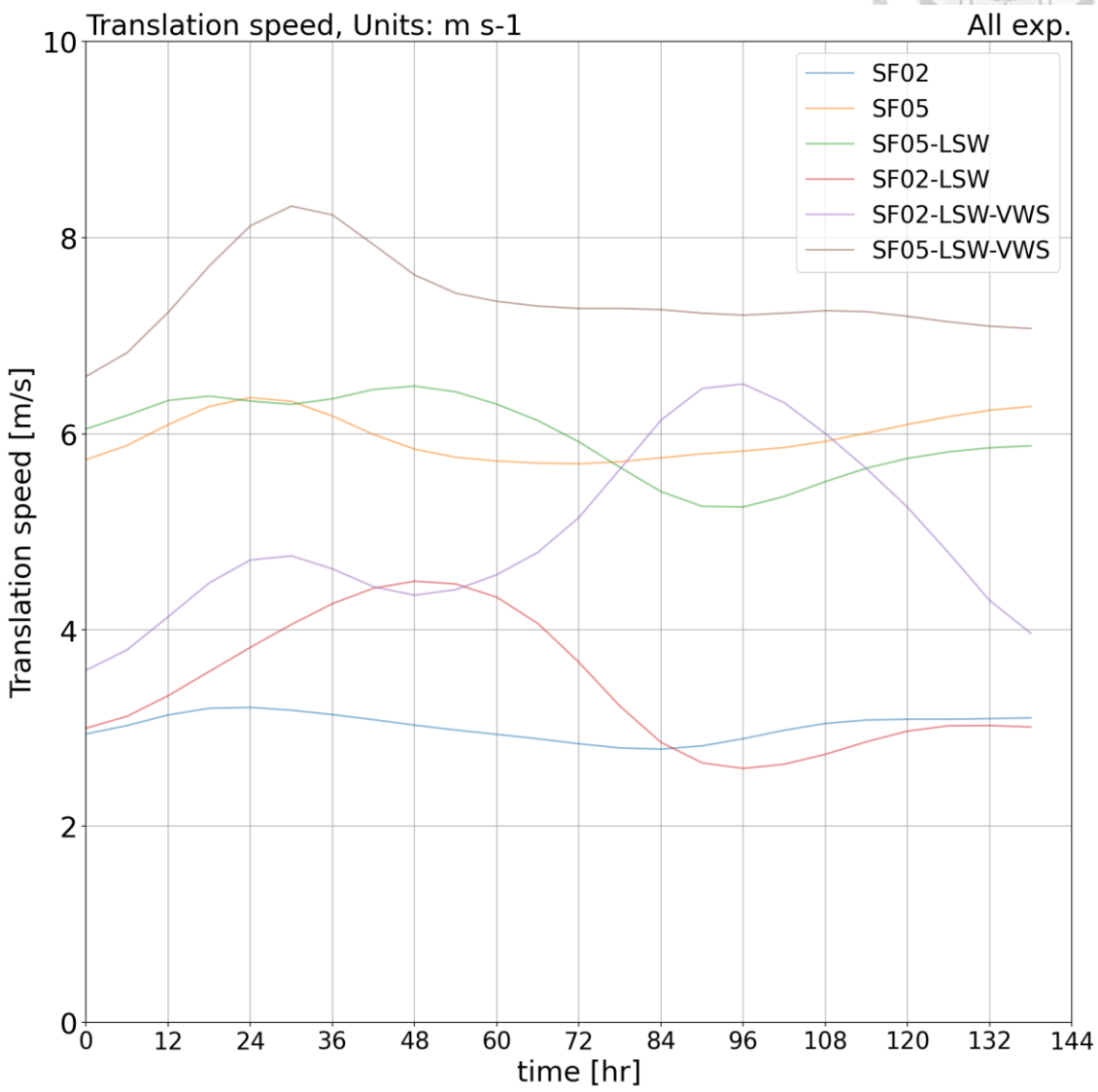

Figure 2.1 Translation speed. Each simulation is represented by T28BLT30

doi:10.6342/NTU202502292

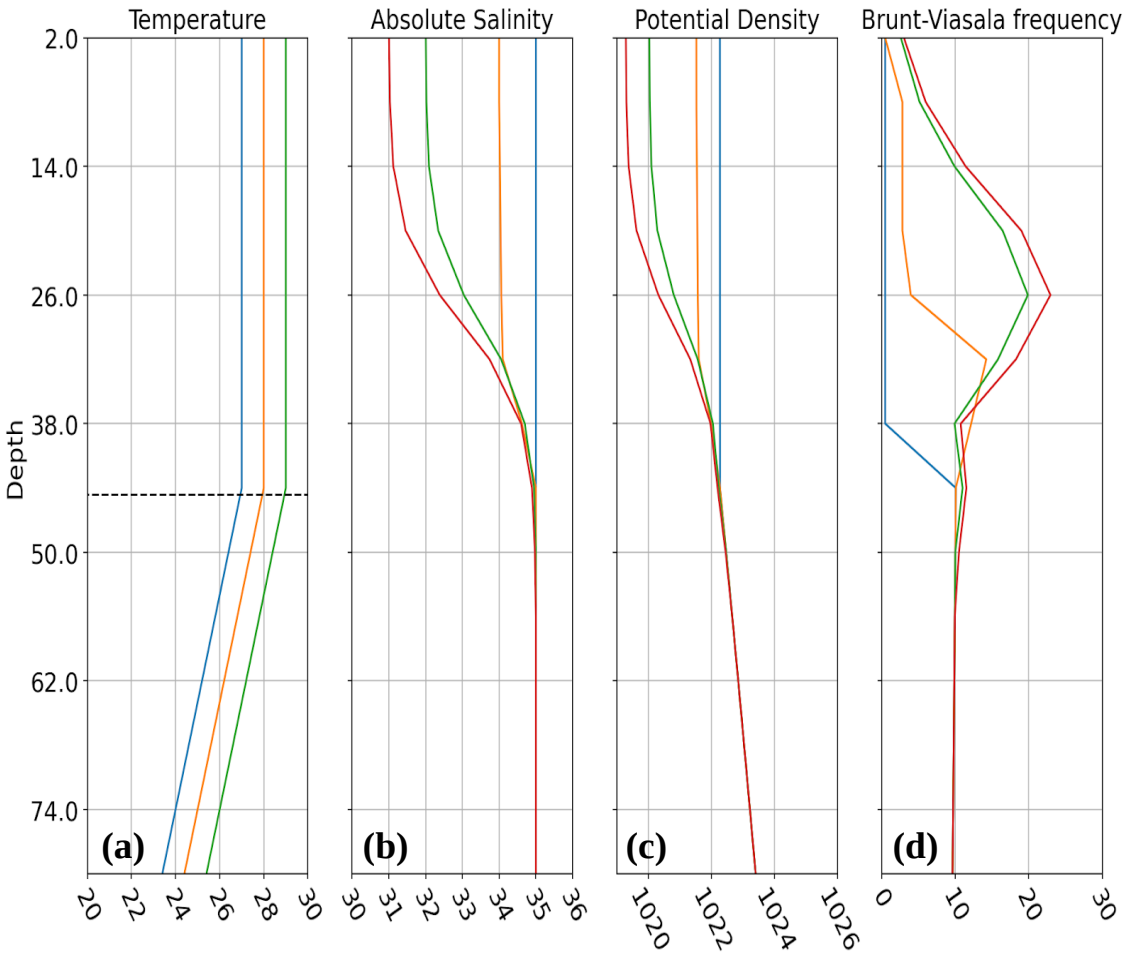

Figure 2.2. Initial ocean profile configuration. (a) Temperature profile: The blue, orange, and green lines represent surface temperatures of 27˚C, 28˚C, and 29˚C, respectively. Temperature lapse rate is 0.1 ˚C m^{-1} below the dashed line at 44 m depth (b) Salinity profile: The blue, orange, green, and red lines correspond to surface salinity levels of 35, 34, 32, and 31 psu, respectively. (c) Potential density profile: Density is depicted as a function of temperature and salinity variations. (d) Brunt-Vaisala frequency: The blue, orange, green, and red lines also indicate barrier layer (BL) thicknesses of 0, 12, 24, and 30 m, respectively.

doi:10.6342/NTU202502292

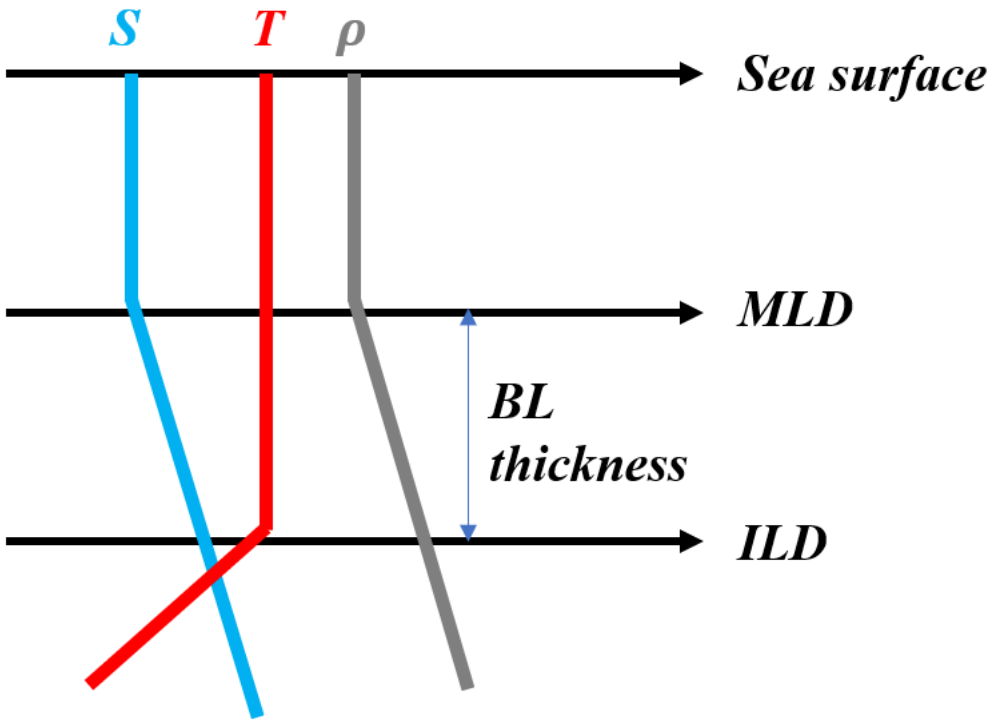

Figure 2.3. Schematic diagram of the ocean structure with the existence of the barrier layer (BL). The thickness of the BL is defined as the difference between the depth of the IL and the ML. Blue, red, and grey line indicate the profile of salinity (S), temperature (T), and density (ρ), respectively.

doi:10.6342/NTU202502292

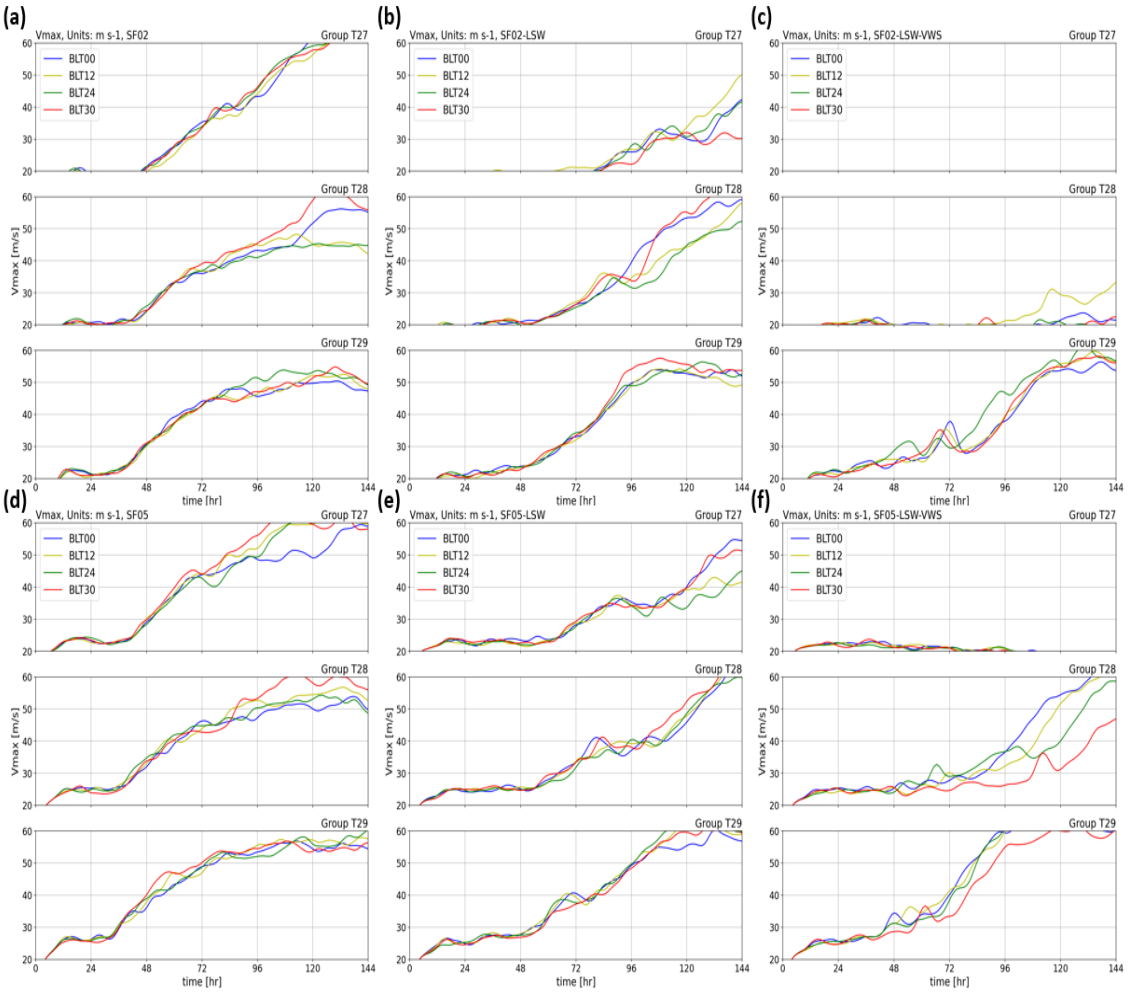

Figure 3.1. Time series of maximum velocity in experiments. Panels represent results from experiments with varying setups: (a) SW02, (b) SW02-LSW, (c) SW02-LSW-VWS, (d) SF05, (e) SF05-LSW, and (f) SW05-LSW-VWS. The blue, yellow, green, and red lines denote barrier layer (BL) thicknesses of 0 m, 12 m, 24 m, and 30 m, respectively. From the top to the bottom represents the results of T27, T28, and T29, respectively.

doi:10.6342/NTU202502292

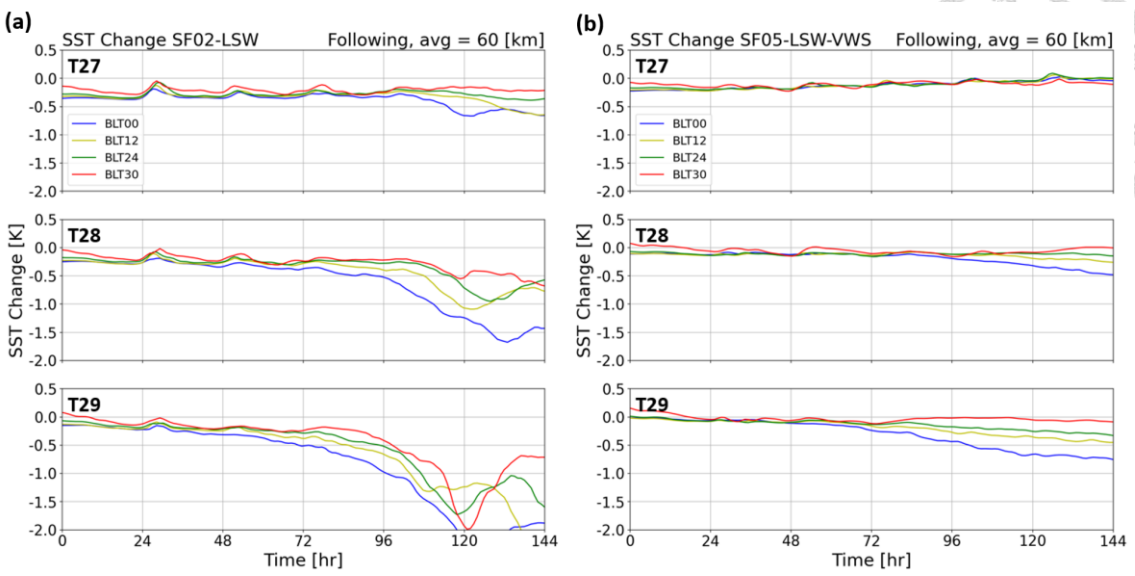

Figure 3.2. Time series of surface sea temperature (SST) changes in experiments. Panels display the results for (left, a) SF02-LSW and (right, b) SF05-LSW-VWS experiments. The blue, yellow, green, and red lines represent barrier layer (BL) thicknesses of 0 m, 12 m, 24 m, and 30 m, respectively. Above results are averaged with a 60km-box following the center of the TCs.

doi:10.6342/NTU202502292

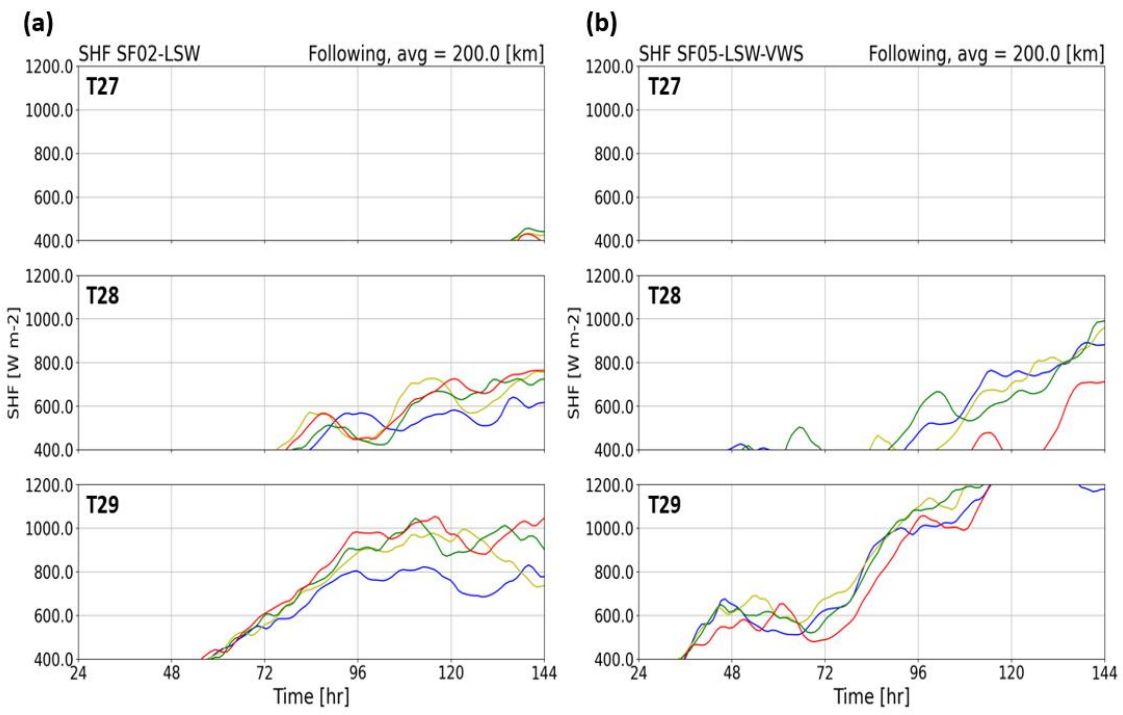

Figure 3.3. Time series of surface heat flux (SHF) in experiments. Similar to Fig. 3.2, but showing the SHF instead. Above results are averaged with a 200km-box following the center of the TCs.

doi:10.6342/NTU202502292

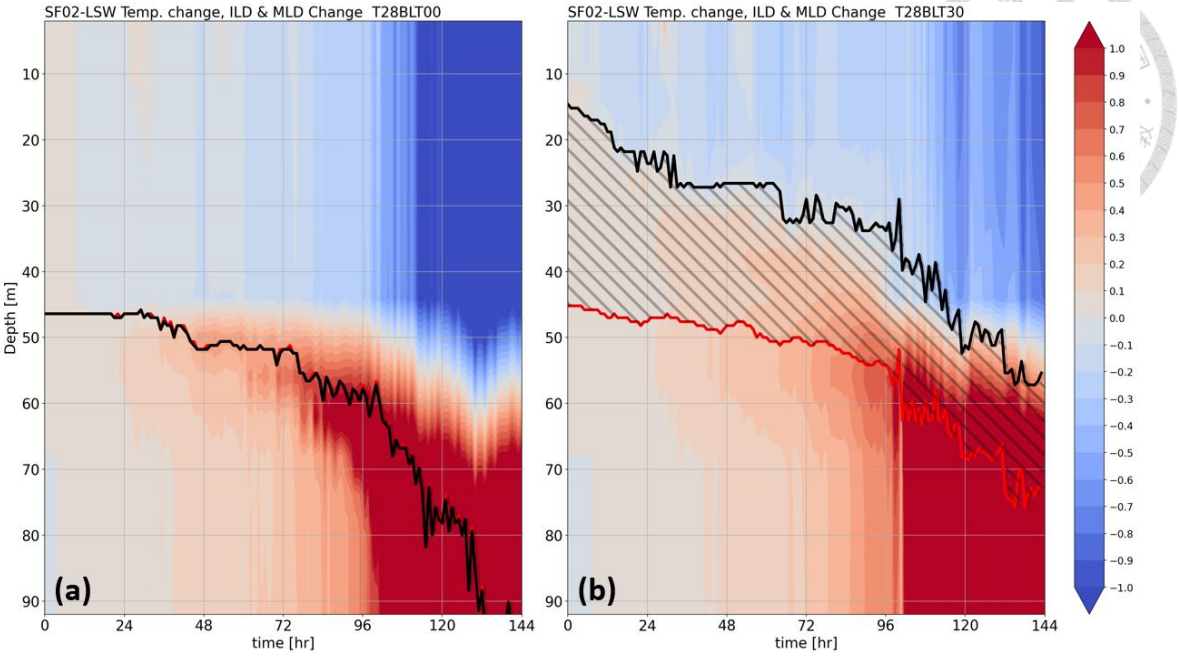

Figure 4.1. Temperature change in the ocean column in BLT00 and BLT30 configurations. Shadings illustrate the temperature changes in experiments SF02-LSW under the T28 scenario, with (left, a) BLT00 and (right, b) BLT30. The red and black lines denote the depths of the mixed layer (ML), isothermal layer (IL), respectively, and the backslash-hatched region denotes the thickness of the barrier layer (BL).

doi:10.6342/NTU202502292

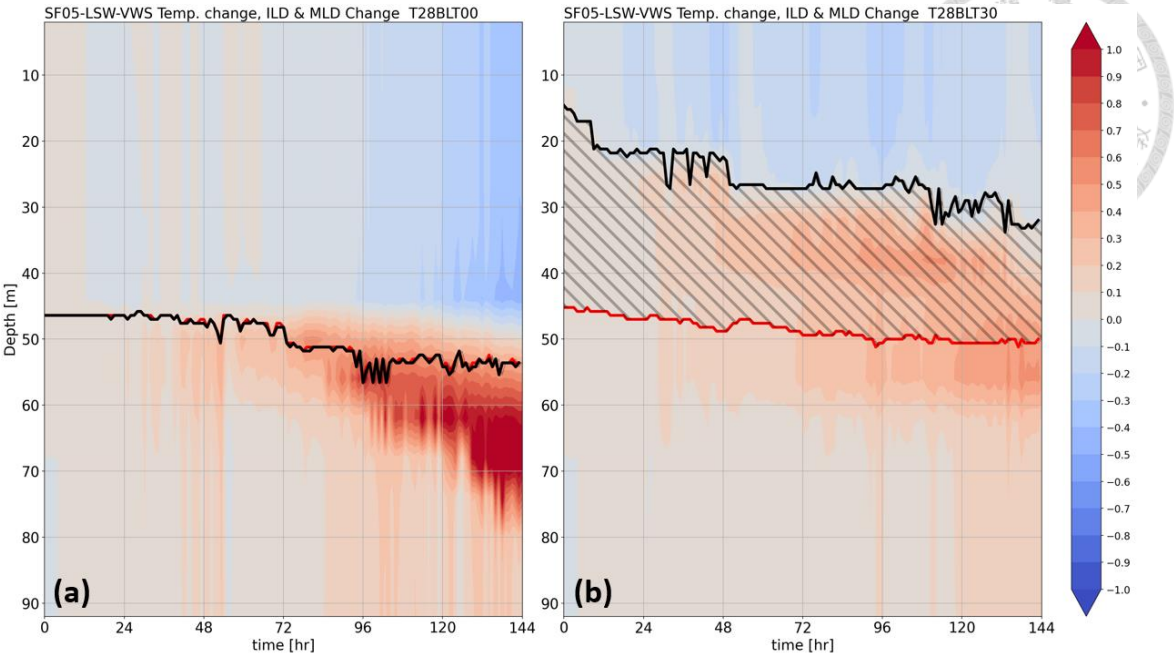

Figure 4.2. Temperature change in the ocean column in BLT00 and BLT30 configurations. Similar to Fig. 4.1, but showing the temperature changes in experiments SF05-LSW-VWS under the T28 scenario instead, with (left, a) BLT00 and (right, b) BLT30.

doi:10.6342/NTU202502292

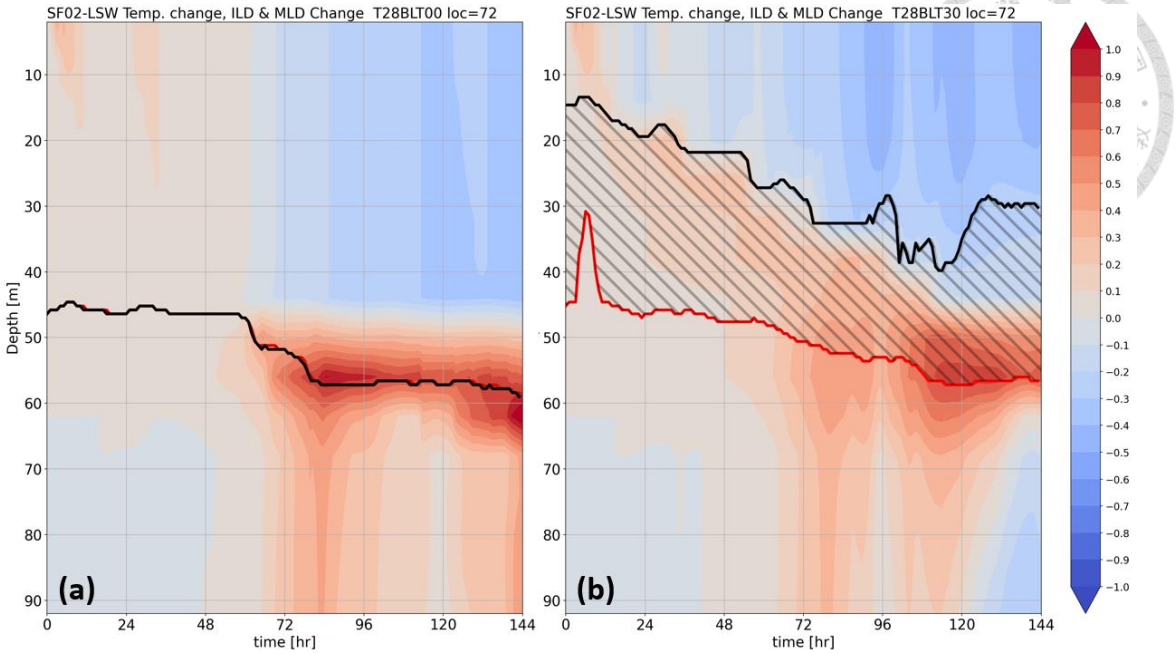

Figure 4.3. Temporal evolution of temperature change along the ocean column at the location of TC passage at the 72-hour mark. The panels illustrate the variation in experiments SF02-LSW under the T28 scenario, with (left, a) BLT00 and (right, b) BLT30. The red and black lines denote the depths of the mixed layer (ML), isothermal layer (IL), respectively, and the backslash-hatched region denotes the thickness of the barrier layer (BL).

doi:10.6342/NTU202502292

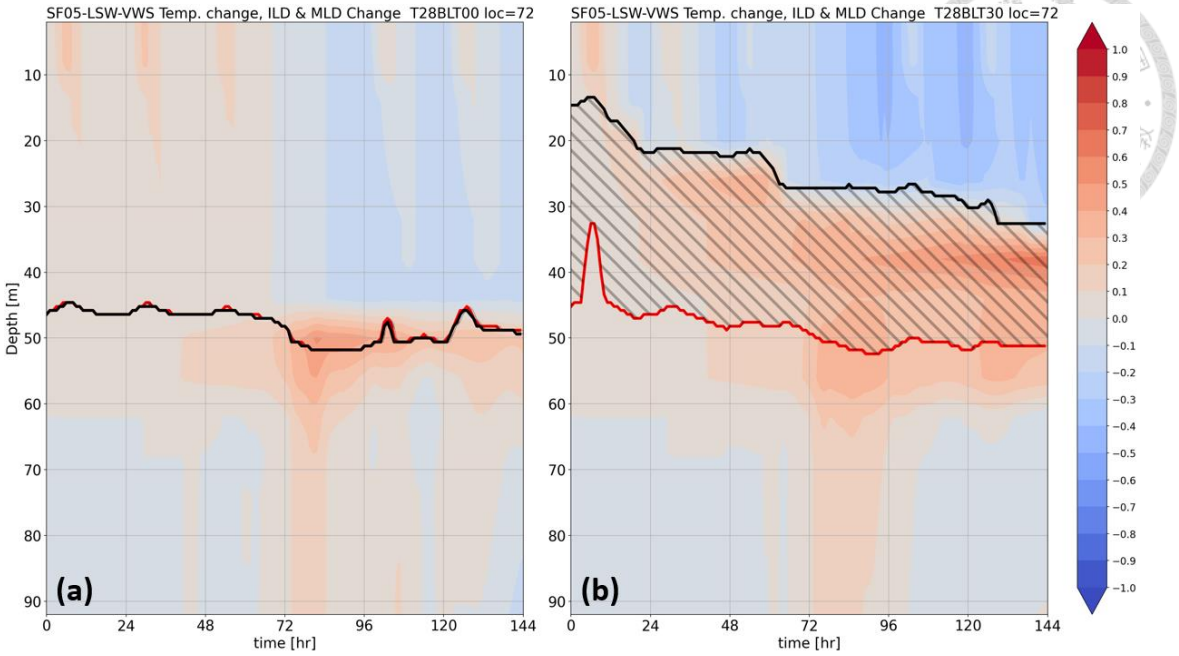

Figure 4.4. Temporal evolution of temperature change along the ocean column at the location of TC passage at the 72-hour mark. Similar with Fig. 4.3, but showing the variation in experiments SF05-LSW-VWS under the T28 scenario instead, with (left, a) BLT00 and (right, b) BLT30.

doi:10.6342/NTU202502292

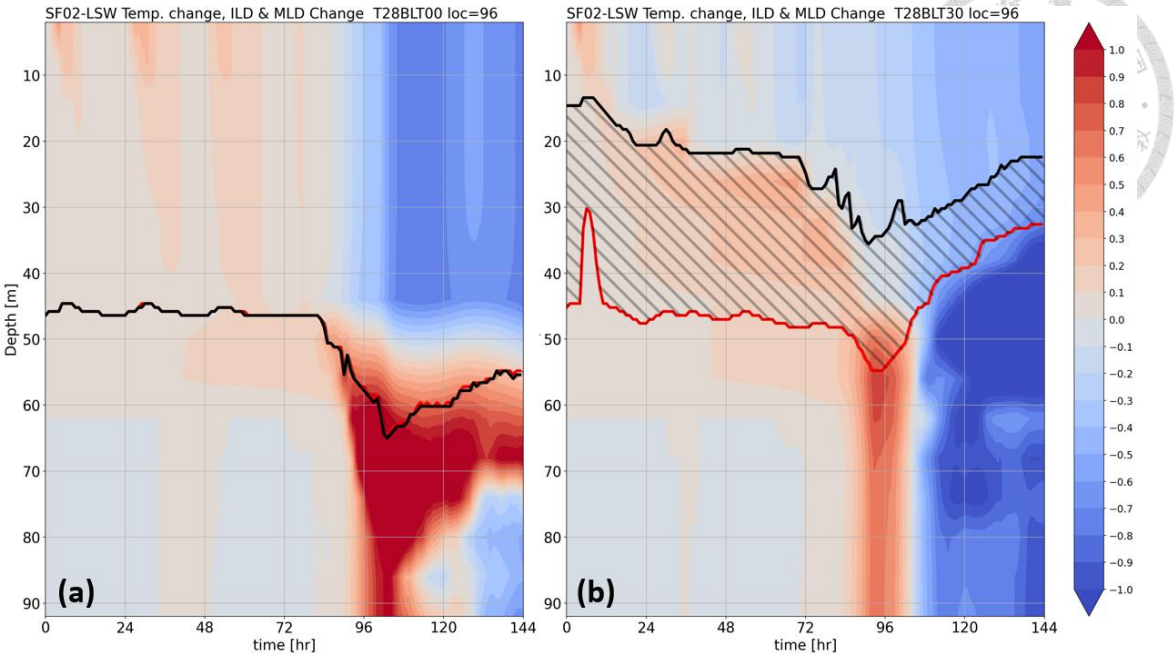

Figure 4.5. Temporal evolution of temperature change along the ocean column at the location of TC passage at the 96-hour mark. The panels illustrate the variation in experiments SF02-LSW under the T28 scenario, with (left, a) BLT00 and (right, b) BLT30. The red and black lines denote the depths of the mixed layer (ML), isothermal layer (IL), respectively, and the backslash-hatched region denotes the thickness of the barrier layer (BL).

doi:10.6342/NTU202502292

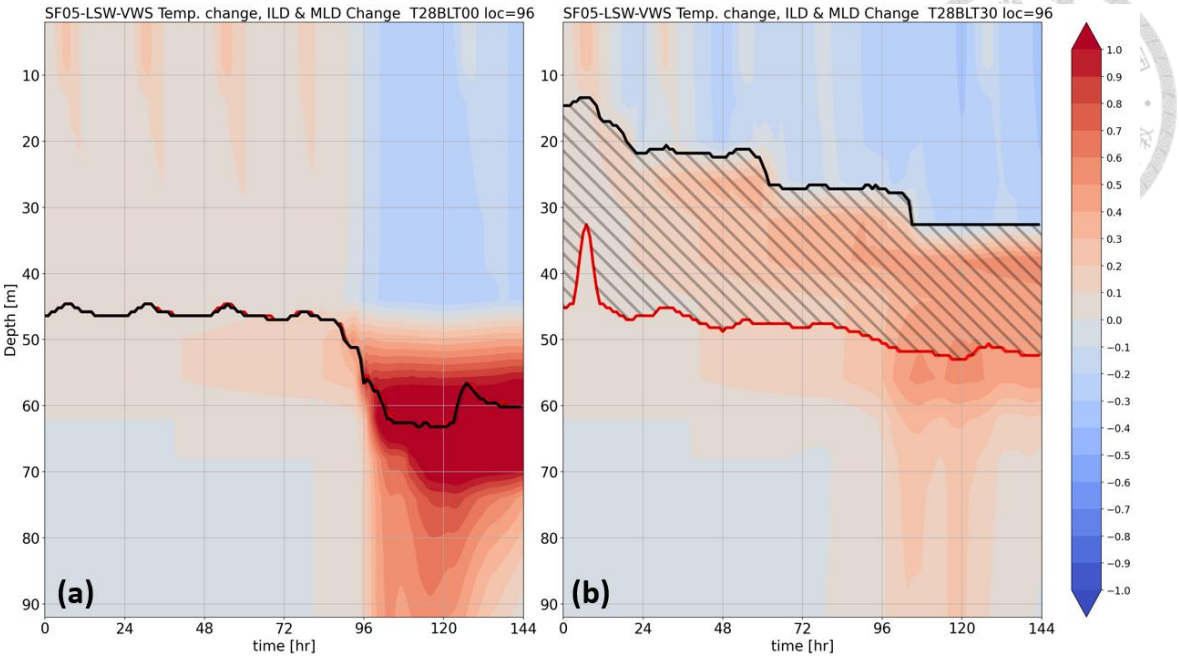

Figure 4.6. Temporal evolution of temperature change along the ocean column at the location of TC passage at the 96-hour mark. Similar with Fig. 4.5, but showing the variation in experiments SF05-LSW-VWS under the T28 scenario instead, with (left, a) BLT00 and (right, b) BLT30.

doi:10.6342/NTU202502292

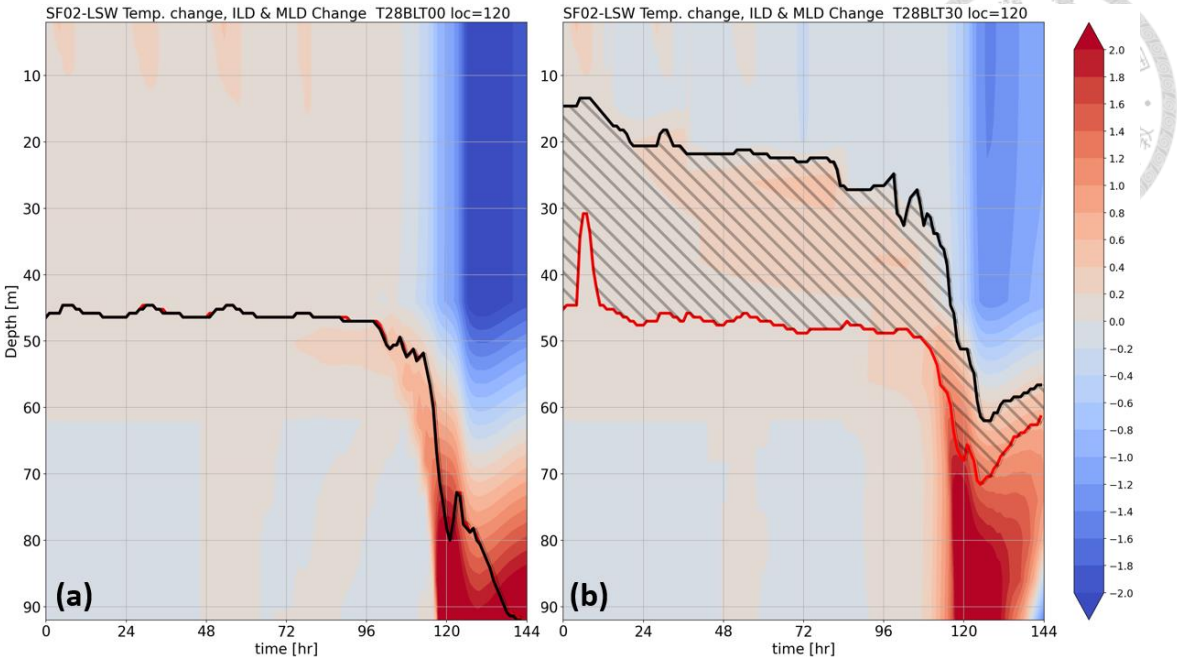

Figure 4.7. Temporal evolution of temperature change along the ocean column at the location of TC passage at the 120-hour mark. The panels illustrate the variation in experiments SF02-LSW under the T28 scenario, with (left, a) BLT00 and (right, b) BLT30. The red and black lines denote the depths of the mixed layer (ML), isothermal layer (IL), respectively, and the backslash-hatched region denotes the thickness of the barrier layer (BL). Notice that the colorbar is different from the others, which is range from -2˚C to 2˚C.

doi:10.6342/NTU202502292

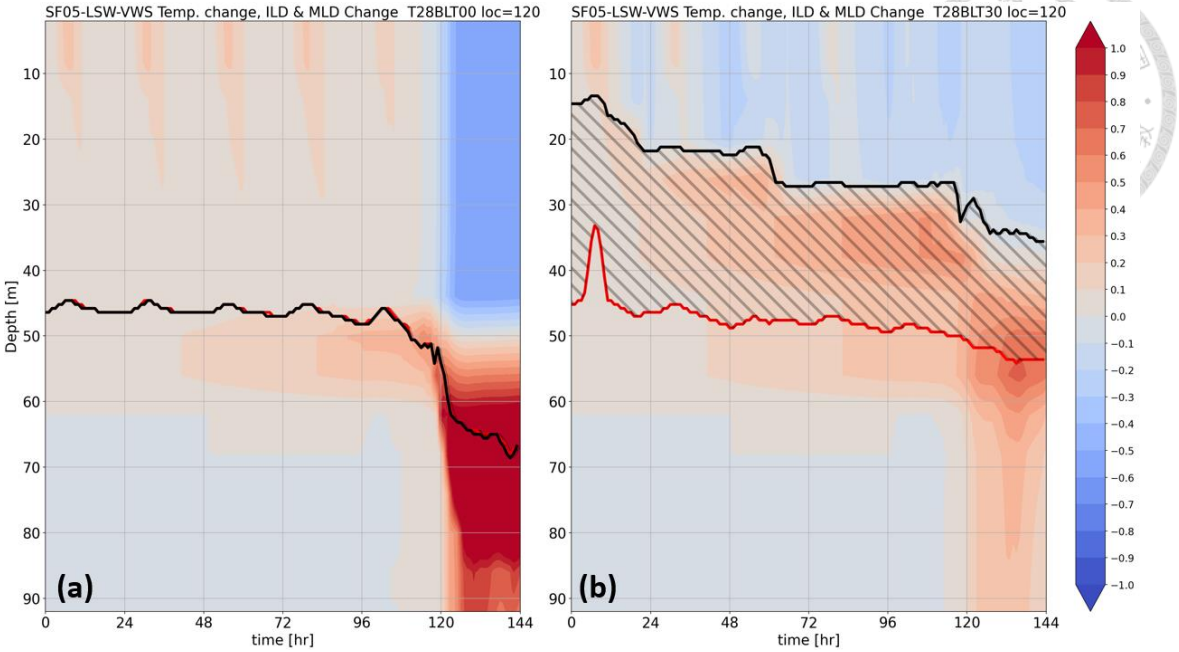

Figure 4.8. Temporal evolution of temperature change along the ocean column at the location of TC passage at the 120-hour mark. Similar with Fig. 4.7, but showing the variation in experiments SF05-LSW-VWS under the T28 scenario instead, with (left, a) BLT00 and (right, b) BLT30.

doi:10.6342/NTU202502292

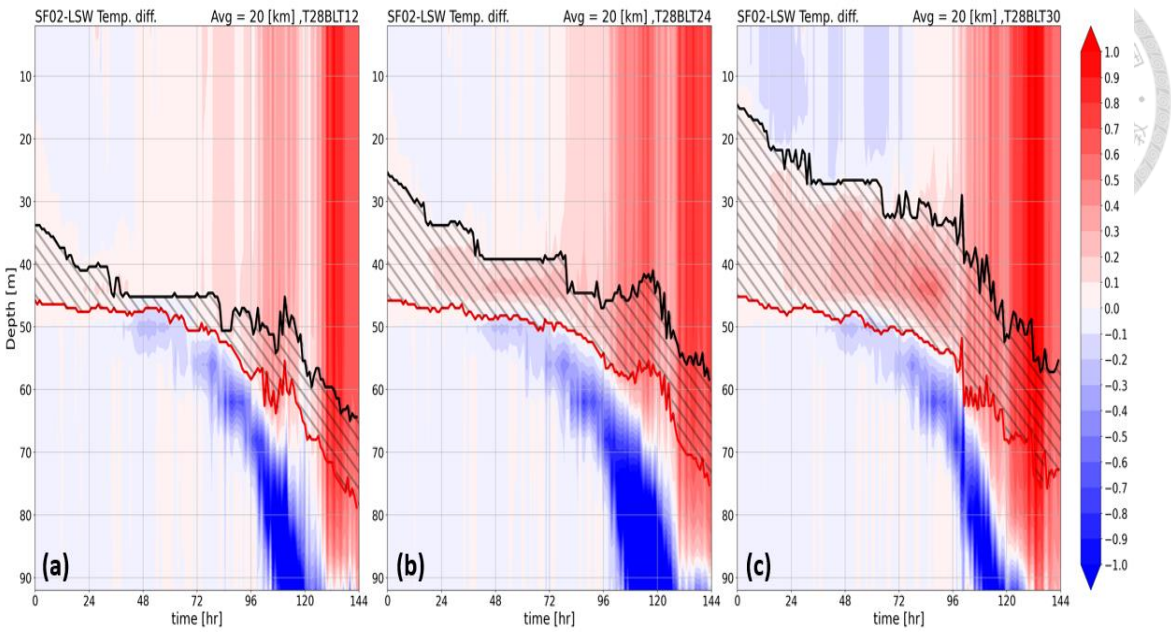

Figure 4.9. Temperature differences between BLT00 and other BL thicknesses in experiments. Panels illustrate the temperature differences in experiments SF02-LSW under the T28 scenario, including comparisons with (left, a) BLT12, (middle, b) BLT24, and (right, c) BLT30. Shading represents the temperature differences relative to BLT00 following the passage of the TCs. The red and black lines denote the depths of the mixed layer (ML), isothermal layer (IL), respectively, and the backslash-hatched region denotes the thickness of the barrier layer (BL).

doi:10.6342/NTU202502292

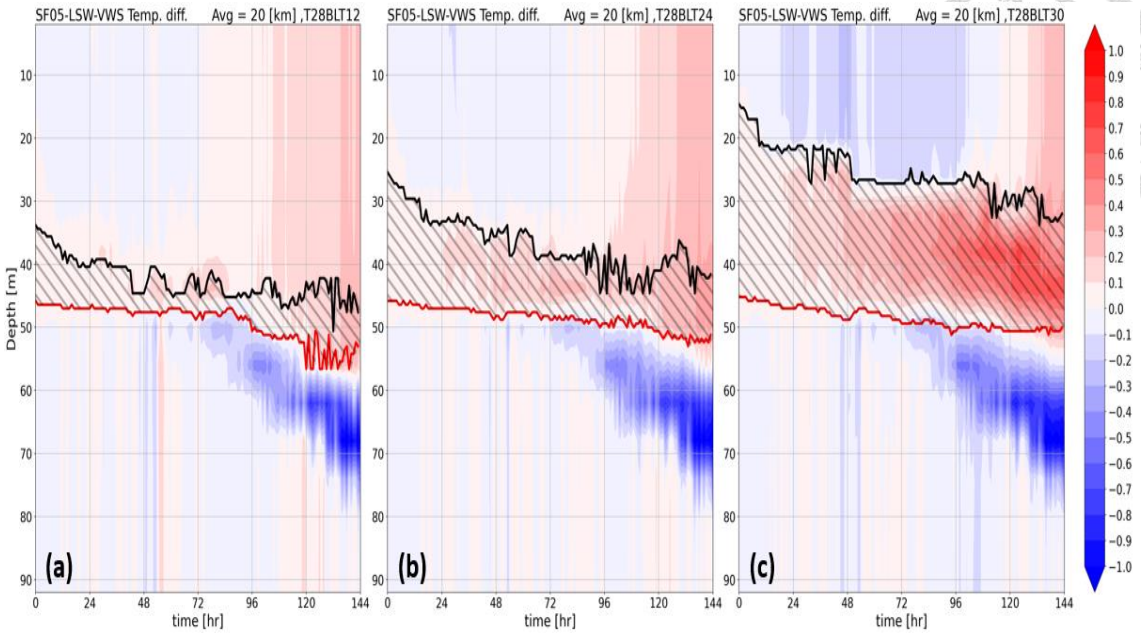

Figure 4.10. Temperature differences between BLT00 and other BL thicknesses in experiments. Similar to Fig. 4.9, but showing the temperature differences in experiments SF05-LSW-VWS under the T28 scenario, including comparisons with (left, a) BLT12, (middle, b) BLT24, and (right, c) BLT30.

doi:10.6342/NTU202502292

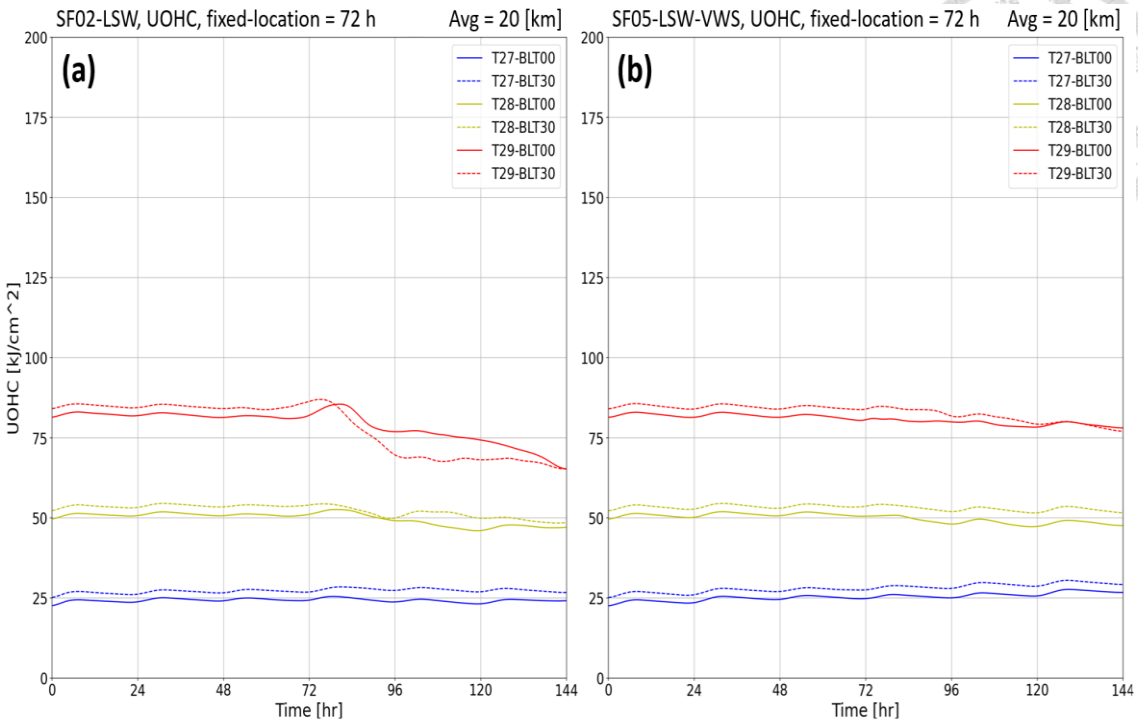

Figure 4.11. Evolution of UOHC in 72-hour fixed-location analysis. Panels depict the evolution of the upper ocean heat content (UOHC) in experiments (left, a) SF02-LSW and (right, b) SF05-LSW-VWS. Blue, yellow, and red lines correspond to groups T27, T28, and T29, respectively. Solid lines represent BLT00, while dashed lines represent BLT30.

doi:10.6342/NTU202502292

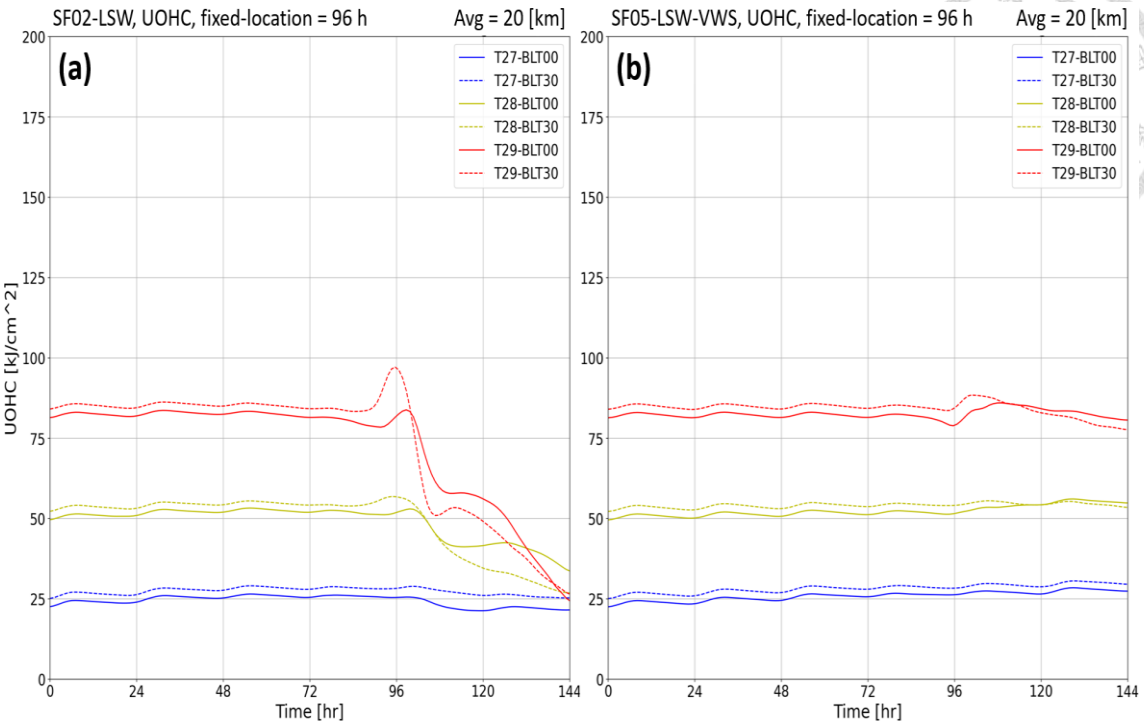

Figure 4.12. Evolution of UOHC in 96-hour fixed-location analysis. Panels depict the evolution of the upper ocean heat content (UOHC) in experiments (left, a) SF02-LSW and (right, b) SF05-LSW-VWS. Blue, yellow, and red lines correspond to groups T27, T28, and T29, respectively. Solid lines represent BLT00, while dashed lines represent BLT30.

doi:10.6342/NTU202502292

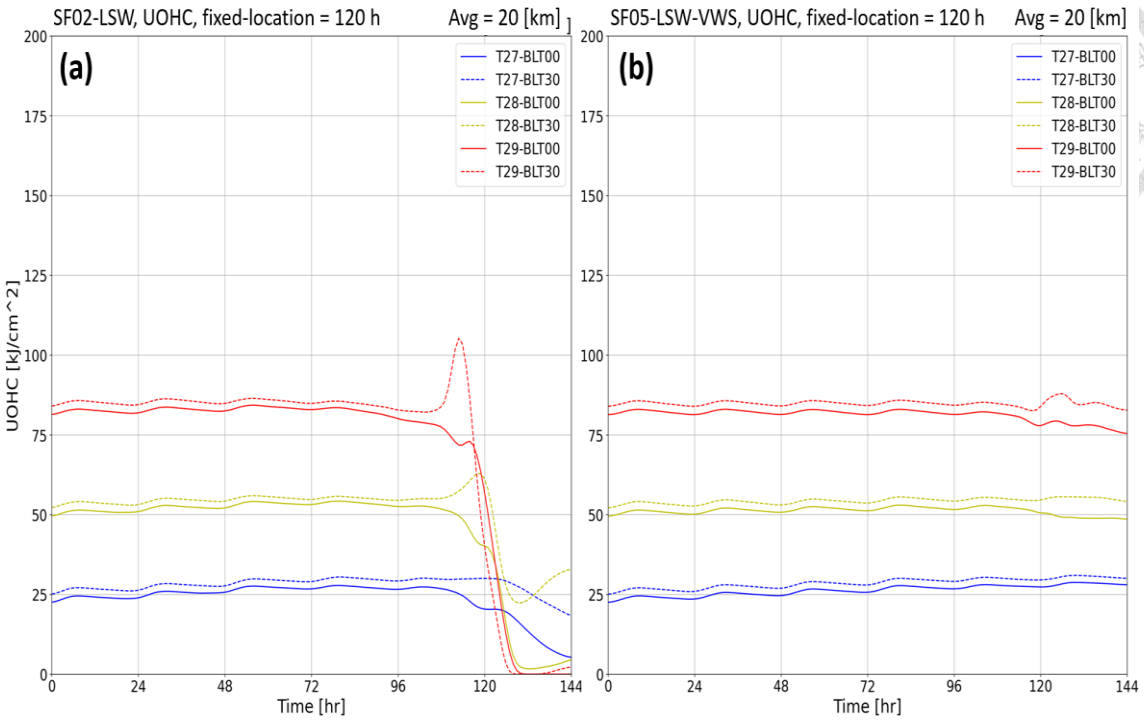

Figure 4.13. Evolution of UOHC in 120-hour fixed-location analysis. Panels depict the evolution of the upper ocean heat content (UOHC) in experiments (left, a) SF02-LSW and (right, b) SF05-LSW-VWS. Blue, yellow, and red lines correspond to groups T27, T28, and T29, respectively. Solid lines represent BLT00, while dashed lines represent BLT30.

doi:10.6342/NTU202502292

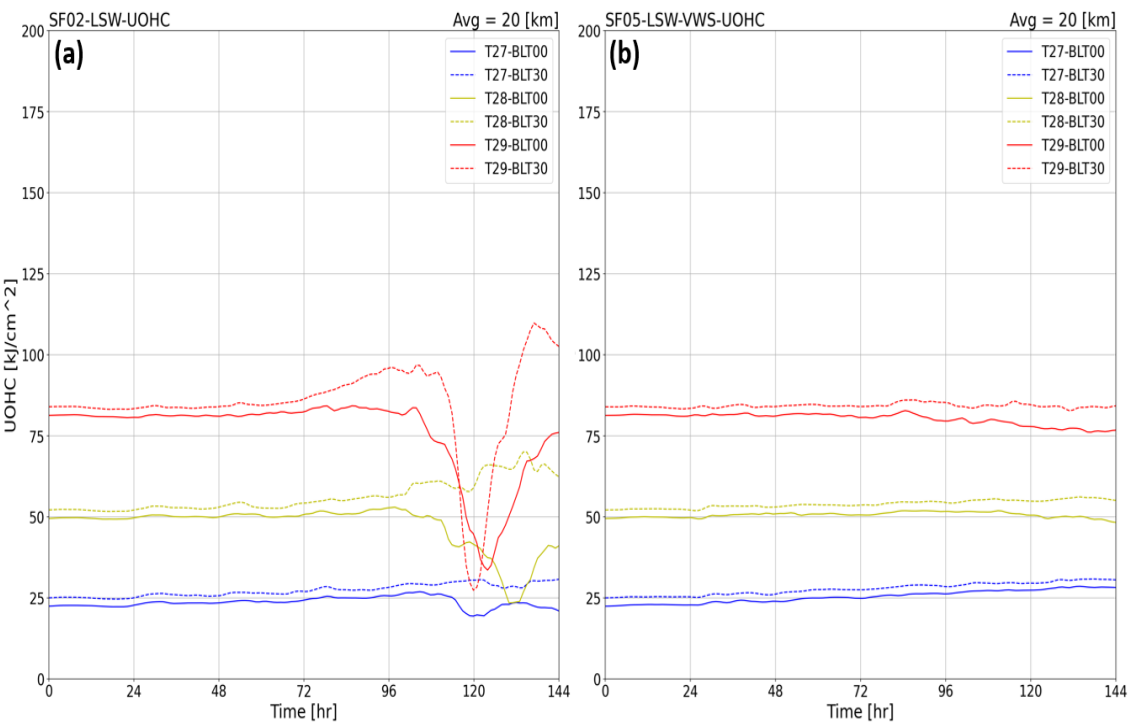

Figure 4.14. Evolution of UOHC under storm-following corrdinate. Panels depict the evolution of the upper ocean heat content (UOHC) in experiments (left, a) SF02-LSW and (right, b) SF05-LSW-VWS. Blue, yellow, and red lines correspond to groups T27, T28, and T29, respectively. Solid lines represent BLT00, while dashed lines represent BLT30.

doi:10.6342/NTU202502292

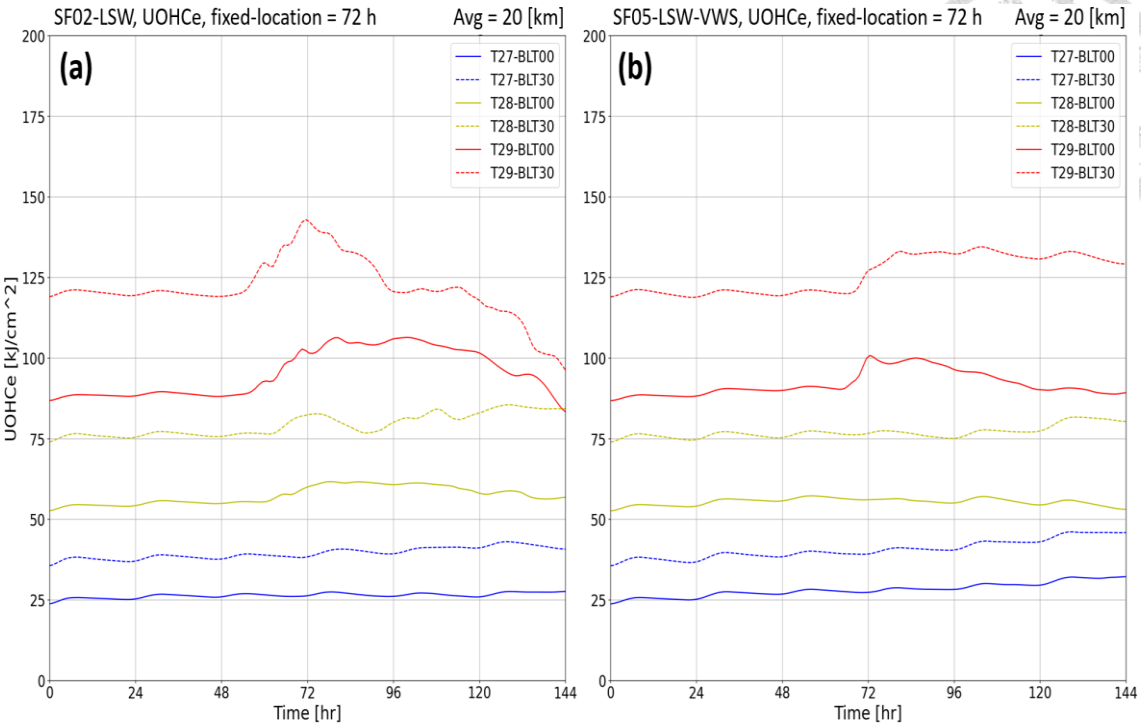

Figure 4.15. Evolution of UOHCe in 72-hour fixed-location analysis. Panels depict the evolution of the equivalent upper ocean heat content (UOHCe) in experiments (left, a) SF02-LSW and (right, b) SF05-LSW-VWS. Blue, yellow, and red lines correspond to groups T27, T28, and T29, respectively. Solid lines represent BLT00, while dashed lines represent BLT30.

doi:10.6342/NTU202502292

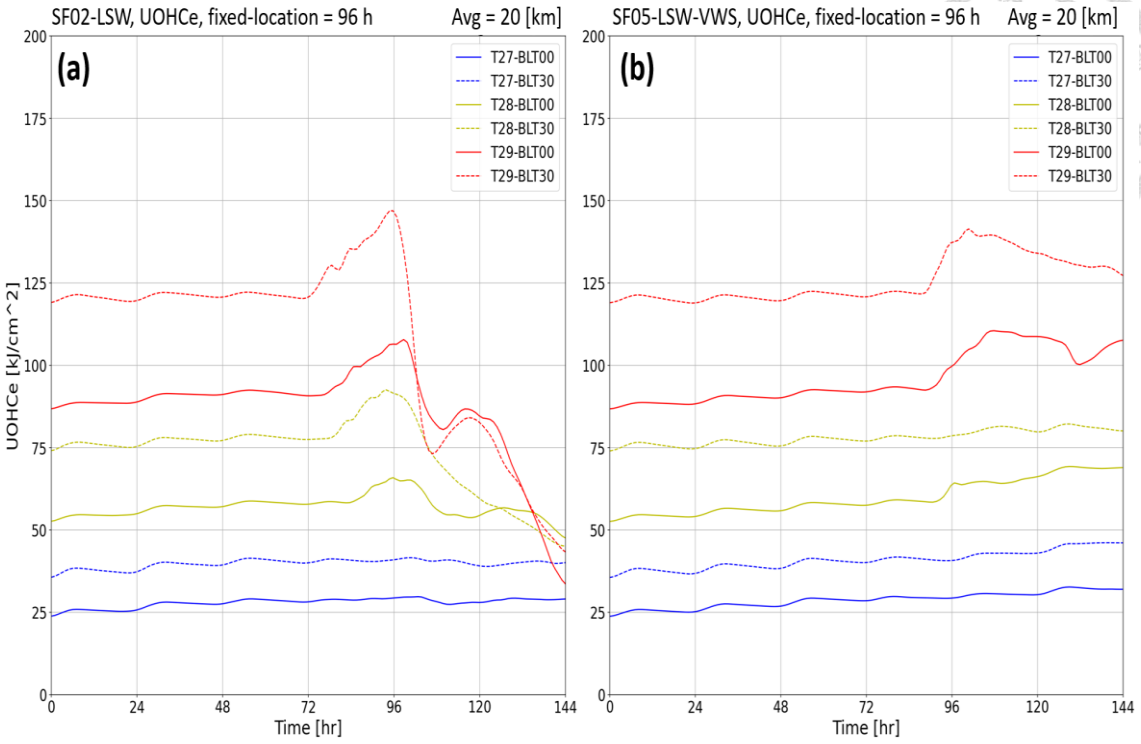

Figure 4.16. Evolution of UOHCe in 96-hour fixed-location analysis. Panels depict the evolution of the equivalent upper ocean heat content (UOHCe) in experiments (left, a) SF02-LSW and (right, b) SF05-LSW-VWS. Blue, yellow, and red lines correspond to groups T27, T28, and T29, respectively. Solid lines represent BLT00, while dashed lines represent BLT30.

doi:10.6342/NTU202502292

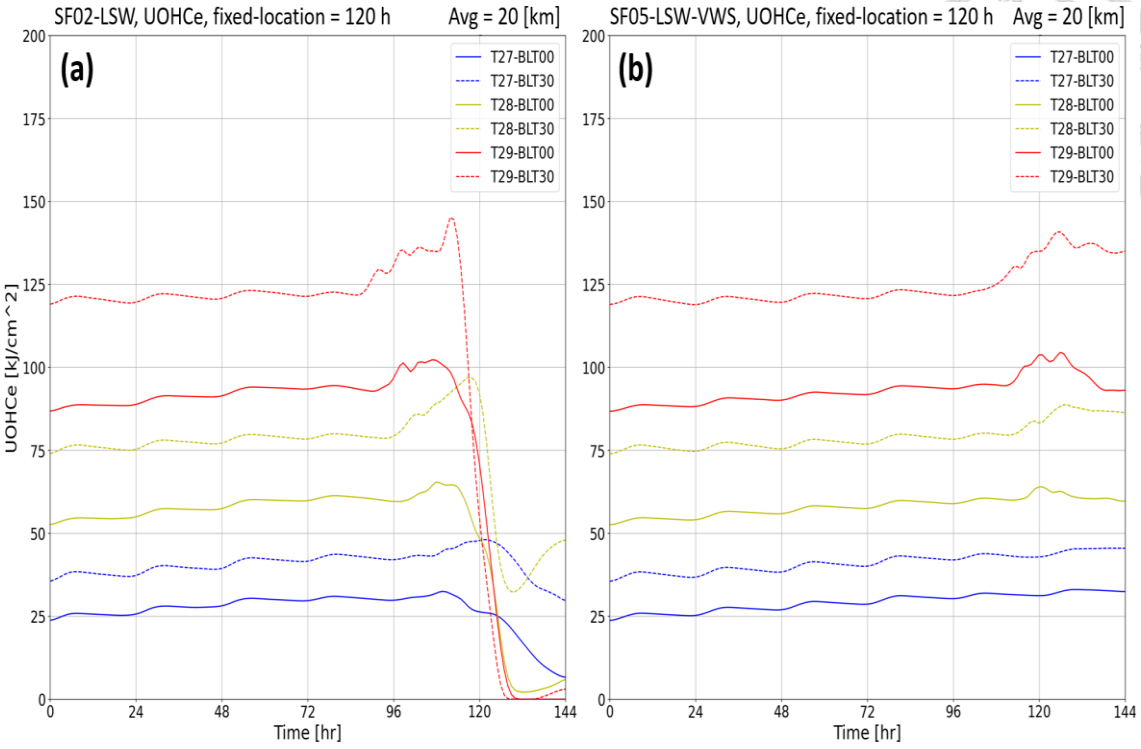

Figure 4.17. Evolution of UOHCe in 120-hour fixed-location analysis. Panels depict the evolution of the equivalent upper ocean heat content (UOHCe) in experiments (left, a) SF02-LSW and (right, b) SF05-LSW-VWS. Blue, yellow, and red lines correspond to groups T27, T28, and T29, respectively. Solid lines represent BLT00, while dashed lines represent BLT30.

doi:10.6342/NTU202502292

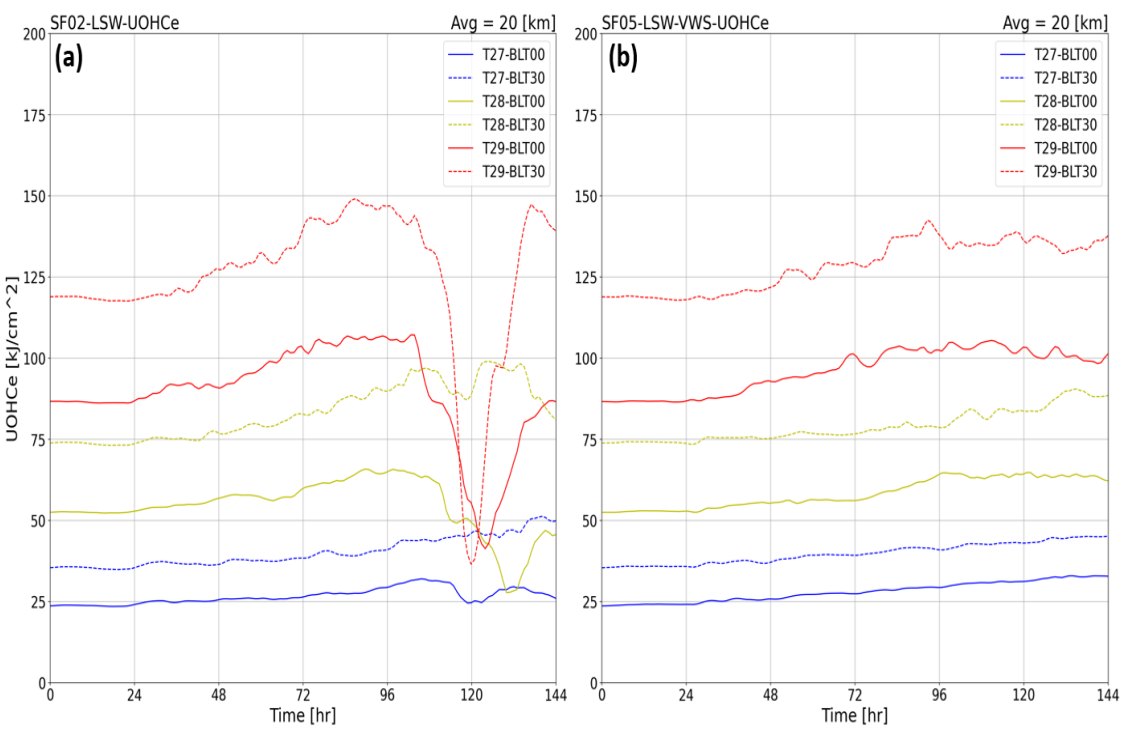

Figure 4.18. Evolution of UOHCe under storm-center following corridinate. Similar to Fig. 4.14, but showing the evolution of UOHCe instead.

doi:10.6342/NTU202502292

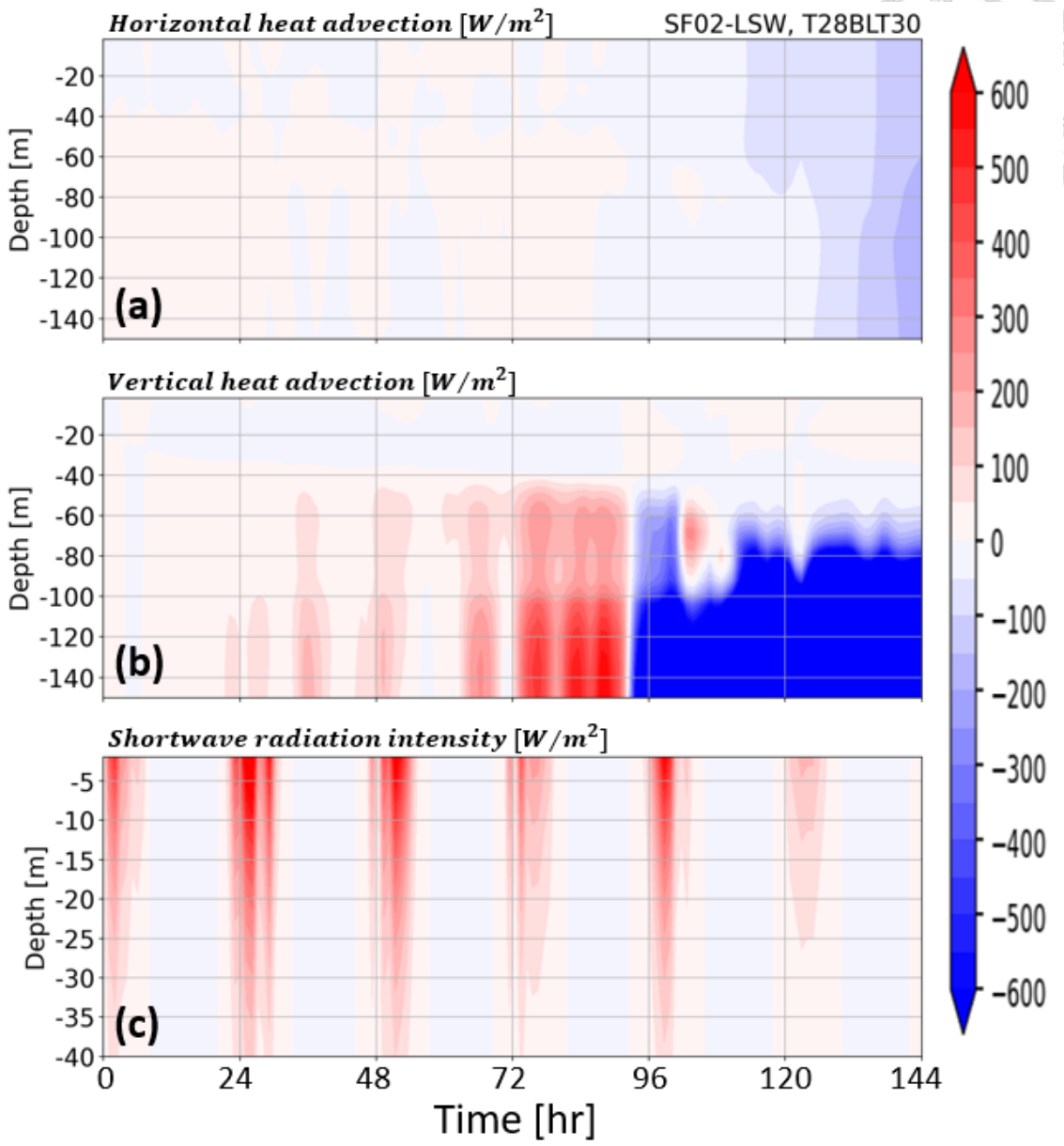

Figure 4.19. Heat budget analysis. The panels illustrate the variation of heat in the experiments SF02-LSW. The shading represents the following: horizontal heat advection (top, a), vertical heat advection (middle, b), and net shortwave radiation (bottom, c).

doi:10.6342/NTU202502292

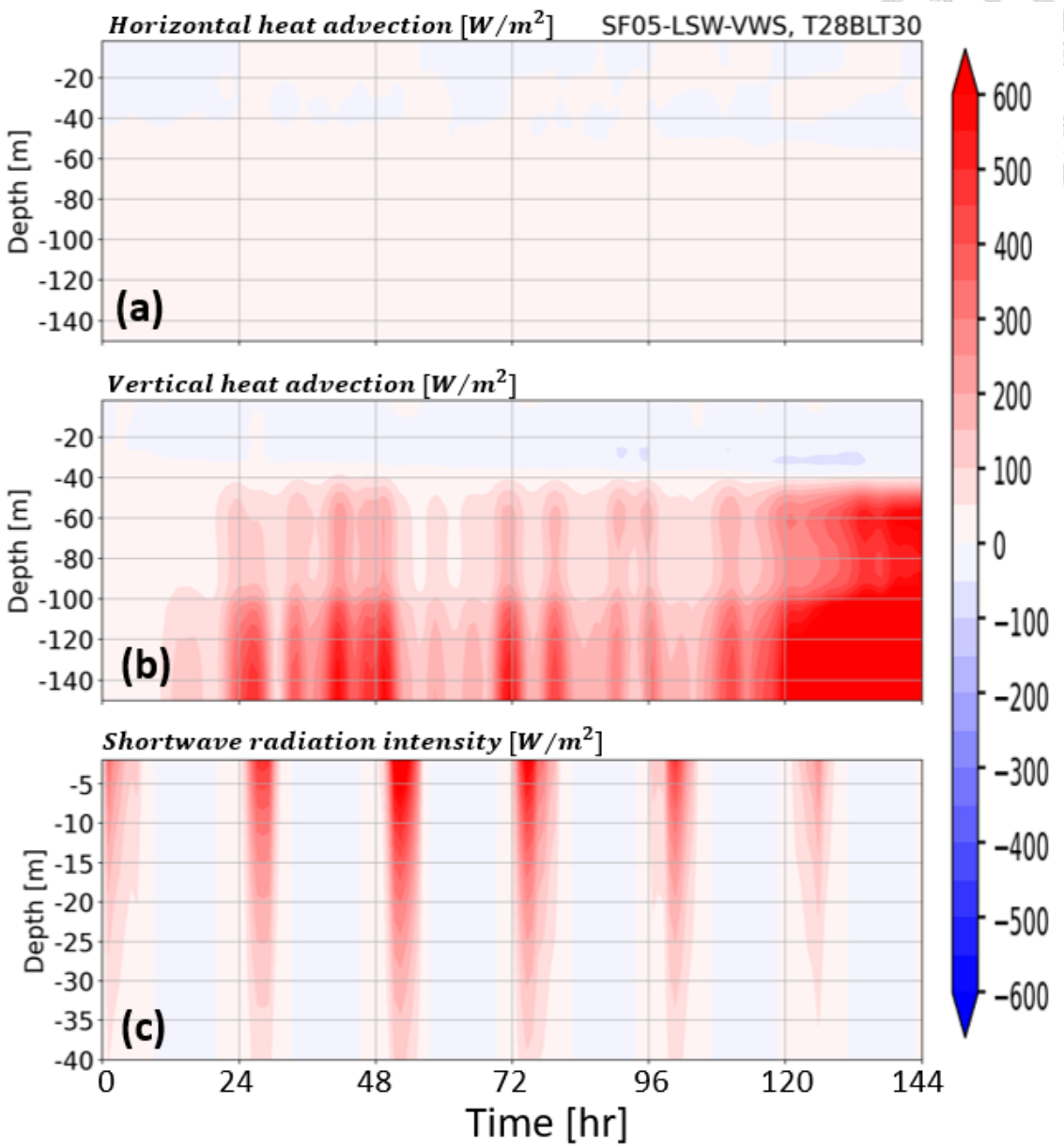

Figure 4.20. Heat budget analysis. Similar to Fig. 4.13, but showing the variation of heat in the experiments SF05-LSW-VWS. The shading represents the following: horizontal heat advection (top, a), vertical heat advection (middle, b), and net shortwave radiation (bottom, c).

doi:10.6342/NTU202502292

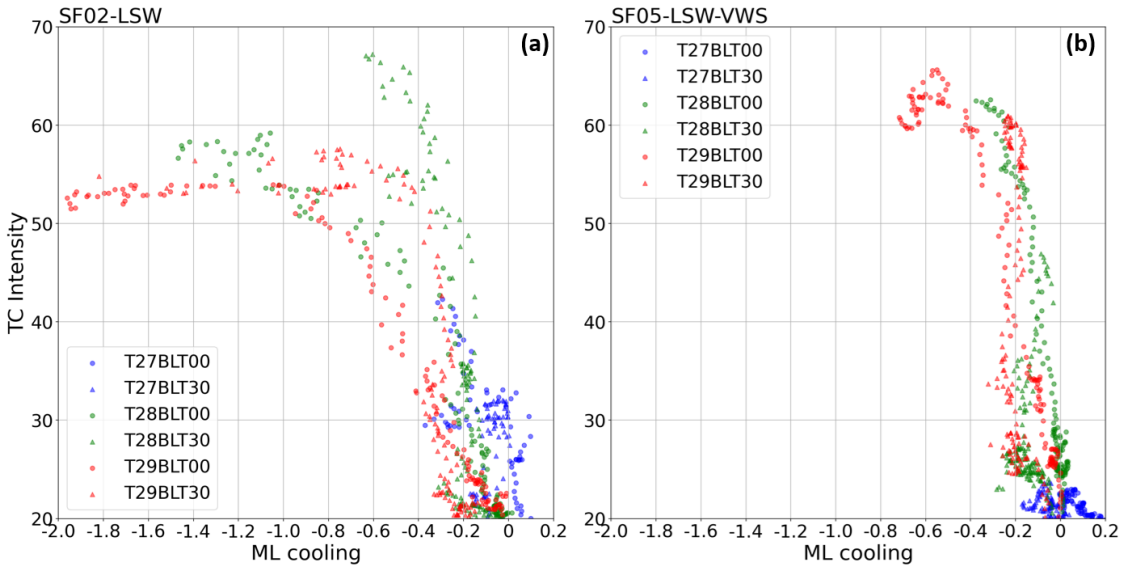

Figure 5.1. Scatter plot between the magnitude of the ML cooling and TC intensity. The panels illustrate the cooling within the ML under corresponding TC intensity for (left, a) SF02-LSW and (right, b) SF05-LSW-VWS. The magnitude of the ML cooling is determined by the difference with the initial ocean thermal structure. Blue, green, and red points represent T27, T28, and T29, respectively. The circle mark and the triangle mark represent BLT00 and BLT30 configurations, respectively.

doi:10.6342/NTU202502292

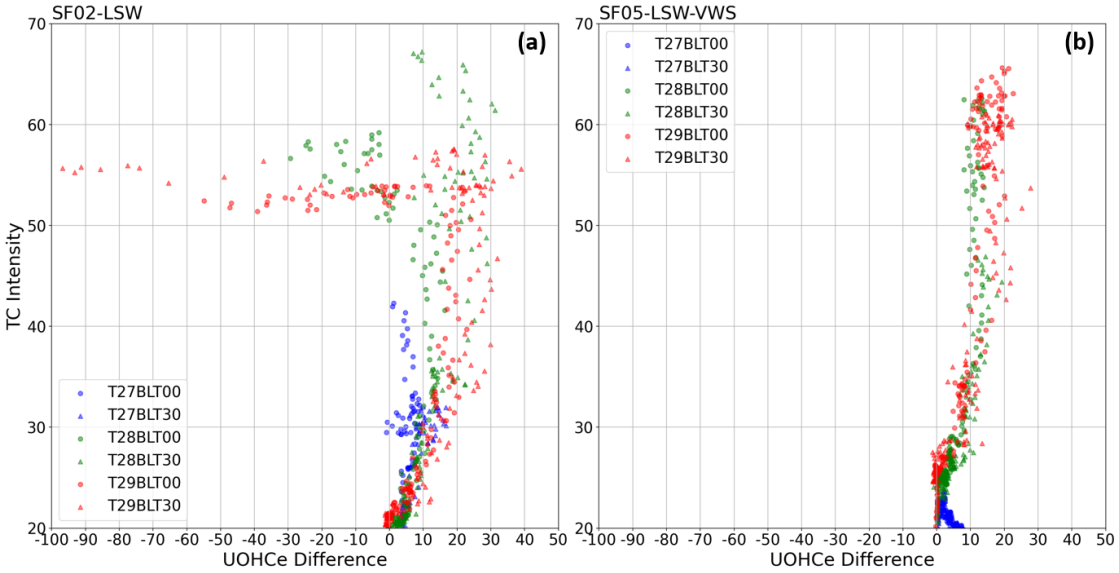

Figure 5.2. Scatter plot between change of the UOHCe and TC intensity. Similar to Fig. 5.1, the panels illustrate the variation of the UOHCe under corresponding TC intensity for (left, a) SF02-LSW and (right, b) SF05-LSW-VWS. Blue, green, and red points represent T27, T28, and T29, respectively. The circle mark and the triangle mark represent BLT00 and BLT30 configurations, respectively.

doi:10.6342/NTU202502292